

Article

# Carbon Surface-Influenced Heterogeneity of Ni and Co Catalytic Sites as a Factor Affecting the Efficiency of Oxygen Reduction Reaction

Marc Florent and Teresa J. Bandosz \* 

Department of Chemistry and Biochemistry, The City College of The City University of New York, 160 Convent Avenue, New York, NY 10031, USA

\* Correspondence: tbandosz@ccny.cuny.edu

**Abstract:** Highly porous carbon black and micro/mesoporous activated carbon were impregnated with cobalt and nickel nitrates, followed by heat treatment at 850 °C in nitrogen. Detailed information about chemistry and porosity was obtained using XPS, XRD, TEM/EDX, and nitrogen adsorption. The samples were used as ORR catalysts. Marked differences in the performance were found depending on the type of carbon. Differences in surface chemistry and porosity affected the chemistry of the deposited metal species that governed the O<sub>2</sub> reduction efficiency along with other features of the carbon supports, including electrical conductivity and porosity. While dissociating surface acidic groups promoted the high dispersion of small metal species, carbon reactivity with oxygen and acidity limited the formation of the most catalytically active Co<sub>3</sub>O<sub>4</sub>. Formation of Co<sub>3</sub>O<sub>4</sub> on the highly conductive carbon black resulted in an excellent performance with four electrons transferred and a current density higher than that on Pt/C. When Co<sub>3</sub>O<sub>4</sub> was not formed in a sufficient quantity, nickel metal nanoparticles promoted ORR on the Ni/Co-containing samples. The activity was also significantly enhanced by small pores that increased the ORR efficiency by strongly adsorbing oxygen, which led to its bond splitting, followed by the acceptance of four electrons.

**Keywords:** porous carbons; Ni- and Co-based catalytic centers; oxygen reduction; surface chemistry; number of electrons transferred



**Citation:** Florent, M.; Bandosz, T.J. Carbon Surface-Influenced Heterogeneity of Ni and Co Catalytic Sites as a Factor Affecting the Efficiency of Oxygen Reduction Reaction. *Nanomaterials* **2022**, *12*, 4432. <https://doi.org/10.3390/nano12244432>

Academic Editors: Elena Sheka and Maria Letizia Terranova

Received: 1 December 2022

Accepted: 7 December 2022

Published: 13 December 2022

**Publisher's Note:** MDPI stays neutral with regard to jurisdictional claims in published maps and institutional affiliations.



**Copyright:** © 2022 by the authors. Licensee MDPI, Basel, Switzerland. This article is an open access article distributed under the terms and conditions of the Creative Commons Attribution (CC BY) license (<https://creativecommons.org/licenses/by/4.0/>).

## 1. Introduction

One of the factors governing the performance of fuel cells is the efficiency of an oxygen reduction reaction, which is determined by the number of electrons transferred as close as possible to four, an onset potential in the most positive range, small Tafel plot slope, and a high current density. In the specific catalytic reactions of oxygen reduction in either acidic or alkane electrolytes H<sub>2</sub>O or OH<sup>-</sup> are formed, respectively. So far, the most efficient catalysts have been those based on noble metals, and platinum dispersed on various conductive forms of carbons is considered as the benchmark of the catalytic performance [1]. However, high costs of this kind of catalysts directed a search for efficient fuel cell electrocatalysts to transition metals [2,3], and even to nonmetal catalysts [4–6]. While the latter are mainly based on carbon materials modified with various heteroatoms including nitrogen, sulfur phosphorus, and boron, the former approach focuses on the catalytic role of Fe, Ni, Co, or Cu species [2,3]. The emphasis is usually on a catalyst chemical and physical form and on its dispersion on a carbon support. Recently, research efforts have been focused on so-called single atom catalysts [7], SAC, where an atomically dispersed metal is chemically coordinated with nitrogen atoms embedded into the carbon matrix [8]. These materials allow the most efficient utilization of catalytic sites and a provide high stability [9]. For formation of SAC the specificity of a carbon support is a very important feature. Its significance is also demonstrated in a separate line of research dedicated exclusively to carbon catalysts, whose performance has been recently summarized in

various reviews [4,5,10–16]. The advantages of these materials in replacing Pt/C are in a sufficient conductivity and in the relative easiness of the modulation of their electronic structure by an introduction of heteroatoms [17–29]. A special emphasis has been placed on nitrogen [19,20], either alone or in combination with sulfur [22,23,27], and oxygen [28], which, by providing basic and positively charged sites to the carbon surface, attracts oxygen as a first step of its reduction process. Another important heteroatom for ORR is sulfur [21], which has been found as advancing the reduction process when located in the proximity of nitrogen-containing centers [29].

Another catalytically important feature of the carbon materials is their porosity, which has recently been indicated as advancing the oxygen reduction process [10,30–41]. This includes the effect of mesopores as mass transport pores [10] and that of micropores as pseudocatalytic centers contributing to reduction of oxygen through providing a strong adsorption potential [34–41]. Moreover, the higher porosity of carbon is often directly linked to the higher structural defects which were also identified as the catalytic ORR centers [16,42,43].

Carbon blacks are a commodity of a highly conductive nature and they have been commonly used as supports for a high dispersion of noble metal-based catalysts [44,45]. Nevertheless, for this purpose rather nonporous carbon blacks, such as Vulcan, have been explored over their highly porous counterparts [46,47]. However, there are reports on carbon blacks' direct usage as transition metal catalyst supports [47–52] and catalysts themselves [41], especially those modified with nitrogen [53,54]. Even though there are numerous reports on the catalytic effects of transition metals on oxygen reduction on various carbon materials [2,8], carbon blacks deserve special attention not only owing to their high electrical conductivity, but also due to the possibility of utilization of their specific porosity to advance ORR [40,41]. Often that porosity effect might have been overseen when the emphasis of reports was on a direct influence of metal catalysts. Nickel and cobalt are considered as the most suitable catalysts for ORR, and since the works of Bagotzky et al. [55,56], many researchers have reported their positive influence on this reaction; examples are references [48,49,52,55–70]. It has been proposed that either single metal atoms coordinated with nitrogen embedded to the carbon matrix [57,58,60,61], metal nanoparticles [59], and oxides [64,66], especially  $\text{Co}_3\text{O}_4$  [52,57] and oxyhydroxide [64], can work as the ORR catalysts. On the other hand, there are also reports claiming that these metals work as the ORR catalysts only when coordinated with nitrogen [68].

Recent works on various forms of carbon materials, including carbon blacks, activated carbons, carbon nanotubes, or carbon aerogels modified with cobalt and nickel as ORR catalysts have reported that the number of electrons transferred in alkaline electrolytes can reach four [60]; the onset potential can even be more positive than that on Pt/C [57,58], and the kinetic current as high as  $8.1 \text{ mA/cm}^2$  [60]. When a catalytic action of both metals is considered, cobalt usually outperforms nickel [67] and NiCo alloys, alone or integrated with their oxides, and have shown an exceptional catalytic activity [69,70].

Published reports on Co and/or Ni-containing carbons as the ORR or bifunctional catalysts mainly link the catalytic activity to the content of metal on the surface and its dispersion, presence of nitrogen providing the coordination sites, and form/chemistry of Co and Ni species. Some of them analyze the effects of catalyst precursors [59]. The most common catalyst supports are porous carbons (either activated ones or their synthetic counterparts) and carbon blacks. While the former, doped with N or undoped, provide a developed surface area promoting the high dispersion of catalytic sites, the high conductivity of the latter is considered as an advantage, which also directed these materials to be used as the Pt catalysts supports. What is often not considered as an advantage of carbon blacks is the high surface area of some specific commercial products, and an example is Black Pearl 2000. Even though Black Pearl carbon blacks have been studied as ORR catalysts and supports with some conflicting results [41,44,68,71], and recently the role of oxygen adsorption in pores of the Black Pearl carbon family has been indicated as affecting the efficiency of ORR [40,41], in our opinion, in the results published so far

there has not been enough emphasis on researching the role of the carbon black surface in promoting the activity of the Co/Ni catalysts for ORR and in providing synergistic activity. Our inspiration for pursuing this angle of research is in our recent results on the excellent performance of this commodity, either unmodified [41] or modified with nitrogen [72], in the oxygen reduction process. To provide deeper insight into this perspective, we analyzed Co and/or Ni modified Black Pearl 2000 catalysts in parallel with those based on commercial wood-based activated carbon BAX-1500 of a highly developed surface area in a micro/mesoporous structure. The results discussed threw new light not only on the nature of active sites affecting ORR, but also on the role of the carbon support in bringing this kind of complex catalytic activity. Our efforts focus on “old” carbon forms to provide relatively broad conclusions and to emphasize the economic aspects of targeting alternative sources of energy.

## 2. Materials and Methods

### 2.1. Materials

Commercial carbon black from Cabot Corporation (Boston, MA, USA), Black Pearls 2000 (referred to as BP), and wood-based activated carbon from Ingevity (North Charleston, SC, USA), BAX-1500 (referred to as BAX) were used as catalysts supports. While BP was used as-received, BAX pellets were first ball-milled and sieved to a particle size below 212  $\mu\text{m}$ . Cobalt nitrate hexahydrate ( $\text{Co}(\text{NO}_3)_2 \cdot 6\text{H}_2\text{O}$ ) and nickel nitrate hexahydrate ( $\text{Ni}(\text{NO}_3)_2 \cdot 6\text{H}_2\text{O}$ ) were used separately or combined in a 1 to 1 mass ratio of the salts to introduce metal-base active phase onto the carbon surface. BAX or BP was first impregnated with an aqueous solution of metal salt using a 1:1 mass ratio of carbon to salt (equivalent to 1:0.2 mass ratio of carbon to metal). After drying, the mixtures were heated at 850  $^\circ\text{C}$  for 30 min, with a heating rate of 10  $^\circ\text{C}/\text{min}$  and under a nitrogen atmosphere (100 mL/min). The samples were then washed in a Soxhlet apparatus until constant pH and dried at 120  $^\circ\text{C}$ . Two series of three samples, BP-Ni, BP-Co, BP-NiCo and BAX-Ni, BAX-Co, and BAX-NiCo were prepared in this way, where the first term designates the type of carbon (BP or BAX) and the second term the kind of metal incorporated (Ni, Co, or a 1-to-1 mix of Ni and Co).

### 2.2. Methods

#### 2.2.1. Surface Characterization

Nitrogen adsorption isotherms measured on an ASAP 2020 (Micromeritics, Norcross, GA, USA) at  $-196$   $^\circ\text{C}$ , after degassing the samples at 120  $^\circ\text{C}$  overnight, were used to calculate a surface area,  $S_{\text{BET}}$  (using the Brunauer–Emmett–Teller theory), and total pore volume  $V_{\text{tot}}$  (from the total amount of nitrogen adsorbed at relative pressure of 0.98). A volume of micropores,  $V_{\text{mic}}$ , was calculated using 2-NLDFT assuming the pore wall heterogeneity [73]. This method was also used to provide pore size distributions. The volume of mesopores  $V_{\text{mes}}$  was calculated from the difference between  $V_{\text{tot}}$  and  $V_{\text{mic}}$ .

Thermogravimetric (TG) and differential TG (DTG) analyses were carried out on an SDT Q600 (TA Instruments, New Castle, DE, USA). The samples were heated up to 1000  $^\circ\text{C}$  with a heating rate of 10  $^\circ\text{C}/\text{min}$  and under a 100 mL/min argon or air flow.

XPS spectra were collected on a Physical Electronics (Chanhasen, MN, USA) PHI 5000 VersaProbe II spectrometer (using an Al  $K\alpha$  X-ray source (50 W, 15 kV, 1486.6 eV) and a take-off angle of 45 $^\circ$ ). A concentric hemispherical analyzer operated in a constant-pass-energy mode, at 29.35 eV, with a 200  $\mu\text{m}$  diameter analysis area. Multipack software was used to deconvolute the spectra.

Resistivity of the materials was measured using a Keithley 2400 Multimeter (Keithley Instruments, Cleveland, OH, USA) on a 0.5  $\times$  0.45 cm gold interdigitated electrode covered with a thin film of carbon.

TEM images were taken with a JEM2100 electron microscope (JEOL, Tokyo, Japan) operated at a 200kV voltage. It is fitted with an Inca Energy Dispersive X-ray Spectrometer (EDX) system used to obtain the elemental maps.

Oxygen adsorption in solution was measured by recording the concentration of dissolved oxygen in 50 mL water using a Hach (Loveland, CO, USA) IntelliCAL LDO probe upon the addition of 250 mg of the carbon sample.

### 2.2.2. Electrochemical Measurements

Electrochemical measurements were carried out with a 0.1 M KOH electrolyte (pH = 13). A three-electrode system was controlled with a WaveDriver 40 bipotentiostat (Pine Research Instrumentation, Durham, NC, USA). A rotating ring-disk electrode (RRDE) with a gold ring and a glassy carbon disk (0.1963 cm<sup>2</sup>) coated with a catalyst ink (a thin film on the carbon disk was made of 33.3 μg of a sample and the same amount of Nafion binder) were used as a working electrode, a graphite rod as a counter-electrode, and a silver/silver chloride electrode (filled with 4 M KCl) as a reference electrode. Potentials  $E_{\text{Ag}/\text{AgCl}}$  measured were converted to potentials versus reversible hydrogen electrode,  $E_{\text{RHE}}$ , using the following formula:

$$E_{\text{RHE}} = E_{\text{Ag}/\text{AgCl}} + 0.199 + 0.59\text{pH} \quad (1)$$

Cyclic voltammetry (CV) curves were measured at a scan rate of 5 mV/s after saturation of the electrolyte solutions with either nitrogen or oxygen gas.

Electrochemically active surface area (ECSA) of the samples was estimated from their double layer capacitance ( $C_{\text{DL}}$ ), assuming that they have a similar specific capacitance  $C_{\text{S}}$  equal to that of carbon black, 27.5 μF/cm<sup>2</sup> [74]:

$$\text{ECSA} = \frac{C_{\text{DL}}}{C_{\text{S}}} \quad (2)$$

$C_{\text{DL}}$  was calculated from the cathodic ( $I_{\text{c}}$ ) and anodic ( $I_{\text{a}}$ ) current measured at different scan rate between 5 and 150 mV/s in a non-faradaic region [75]:

$$C_{\text{DL}} = \frac{I_{\text{c}} + I_{\text{a}}}{2\nu} \quad (3)$$

Linear sweep voltammetry (LSV) curves were recorded at various rotation speeds ( $\omega$ , between 400 and 2000 rpm) in oxygen-saturated electrolytes while keeping the ring at a constant potential of 1.07 V vs. RHE. They were corrected for any capacitive currents by subtracting the background LSV curves measured in oxygen-free electrolytes.

The kinetic current was calculated from the LSV curves, using the Koutecky–Levich Equation (3) [75]:

$$\frac{1}{I_{\text{D}}} = \frac{1}{I_{\text{l}}} + \frac{1}{I_{\text{k}}} = \frac{1}{B\omega^{1/2}} + \frac{1}{I_{\text{k}}} \quad (4)$$

where  $I_{\text{D}}$ ,  $I_{\text{l}}$ , and  $I_{\text{k}}$  are the disk, diffusion limited, and kinetic currents, respectively. They were divided by the carbon disk area, 0.1963 cm<sup>2</sup>, to obtain the corresponding current densities  $J_{\text{D}}$ ,  $J_{\text{l}}$ , and  $J_{\text{k}}$ .

The onset potential was calculated from the LSV curves measured at 2000 rpm using the unbiased second derivative method [76], and the number of electrons transferred,  $n$ , and the percentage of H<sub>2</sub>O<sub>2</sub> produced from Equations (4) and (5), respectively [75]:

$$n = \frac{4I_{\text{D}}}{I_{\text{D}} + \frac{I_{\text{R}}}{N}} \quad (5)$$

$$\% \text{H}_2\text{O}_2 = \frac{200 \frac{I_{\text{R}}}{N}}{I_{\text{D}} + \frac{I_{\text{R}}}{N}} \quad (6)$$

where  $I_{\text{D}}$  and  $I_{\text{R}}$  are the disk and ring currents, respectively, and  $N$  the collection efficiency of the ring-disk electrode is equal to 25.6%.

The Tafel plot of the potential as a function of  $\log(|J_k|)$  was built in a region close to the onset potential and the slope was obtained by a linear fit.

The stability of the samples was evaluated by chronoamperometry at the potential of a maximum oxygen reduction current, with a constant  $O_2$  flow through the electrolyte, for 24 h.

An ethanol crossover effect was tested by measuring the change of a current at the potential giving a maximum oxygen reduction current, upon addition of 2.5 mL of methanol into 60 mL of the electrolyte solution.

### 3. Results and Discussion

Figure 1 presents the comparison of the CV curves collected in the oxygen and nitrogen saturated electrolytes, where oxygen reduction humps are clearly seen with differences in their intensity and the positions of hump minimum/maximum currents. While the oxygen reduction process is better defined for the BP series, a capacitive behavior is more pronounced for the BAX series.

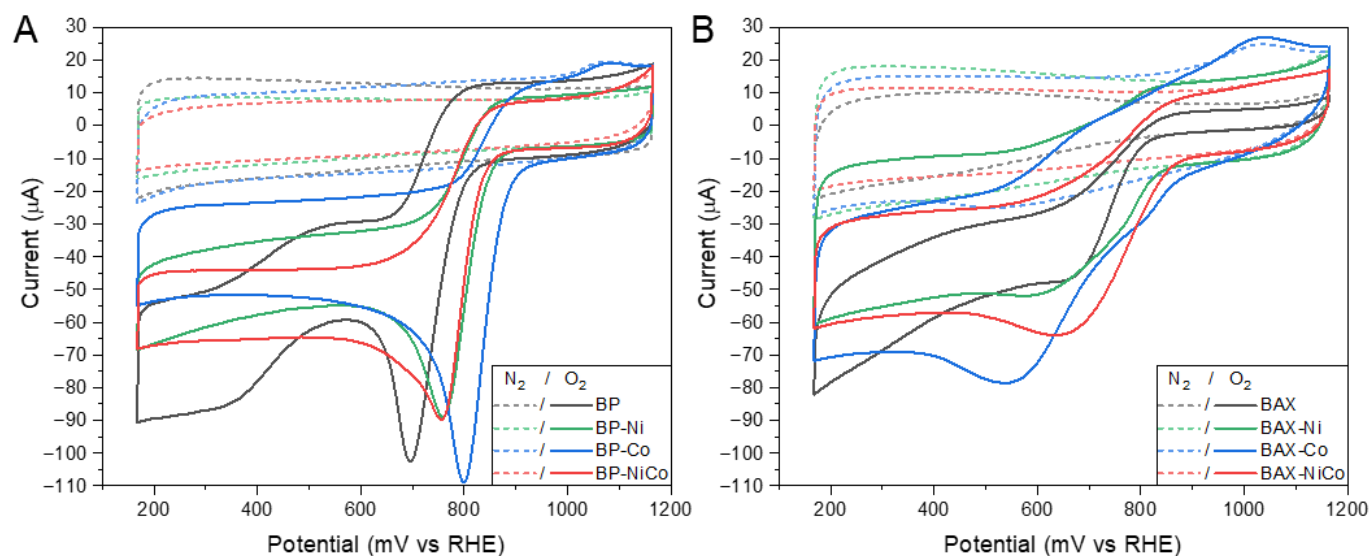


**Figure 1.** CV curves in oxygen and nitrogen saturated electrolytes for the BP (A) and BAX (B) series.

As expected, LSV curves (Figure S1 of the Supplementary Information) show that the current depends on a rotation rate, especially for the BP series, which is typical for a mixed kinetic-diffusion control process. Current densities at 2000 rpm are compared in Figure 2. The modification of BP with metals significantly improved the performance (Figure 2A). While the LSV curve of the initial BP sample exhibits typical two waves characteristic for porous carbons [32], the modification with metals markedly changed the shapes of the LSV curves, making them similar to that measured on Pt/C. Interestingly, the current density measured on BP-Co exceeds that of the platinum-based catalyst of about  $1 \text{ mA/cm}^2$  ( $6.3$  vs.  $5.3 \text{ mA/cm}^2$ ). That current density is higher than those measured on carbon blacks modified with cobalt reported in the literature [52,71]. For example, on Black Pearls 2000 with deposited  $\text{Co}_3\text{O}_4$  the current density reached  $5.6 \text{ mA/cm}^2$  [52], and on the same carbon black modified with cobalt acetate  $4.5 \text{ mA/cm}^2$  [71]. A similar value of the current density ( $6.18 \text{ mA/cm}^2$ ) was reported on carbon black with deposited carbonized  $\text{Co}^{2+}$ ,  $\text{Zn}^{2+}$ , and 2-methylimidazole [57]. The current density of BP-NiCo is between those for the Co- and Ni-modified samples, which might suggest the predominant effect of the cobalt species on the ORR activity on these samples. The onset potential is reported as that calculated from the unbiased second order discrete differentiation method (SODDM) [75]. For the sake of discussion, we also reported a half wave potential (Figure 2B). For BP-Co, which is the best-performing sample, it is  $80 \text{ mV}$  less positive than that on Pt/C, and the other two samples show values lower of  $115 \text{ mV}$  when compared to Pt/C, with BP-Ni as the



worst-performing catalyst. Even though, due to various approaches used in the literature to deliver onset potential values discussed in detail in Ref. [76], the direct comparison of this quantity reported might be biased, it is important to mention that the introduction of Co species led to the onset potential of ORR up to 85 mV more positive than that on the unmodified sample. Liu et al. reported the onset potential of 860 mV on amide grafted and modified with cobalt Vulcan XC-72, while on Black Pearls 2000 with  $\text{CoO}_x$  only 750 mV was measured [71]. Among other results reported in the literature, on nickel porphyrin-modified carbon fiber the onset potential was 820 mV [77], on tetraphenolphthaloin cobalt (II) phthalocyanine polymer modified multiwalled carbon nanotubes it was 803 mV [78], and on atomically dispersed cobalt on N-doped carbon frameworks - 870 mV [60]. In terms of the kinetic current density calculated using the Koutecky–Levich Equation (Figure 2C), BP-Co shows an exceptional performance, reaching  $\sim 130 \text{ mA/cm}^2$ , which is much higher than the kinetic current density measured on Pt/C ( $\sim 35 \text{ mA/cm}^2$ ). The results obtained on BP-Co are better than those reported in the literature on Co-modified carbon, [52,57,71,78] and even on those where SAC were directly targeted [15,59,79,80].

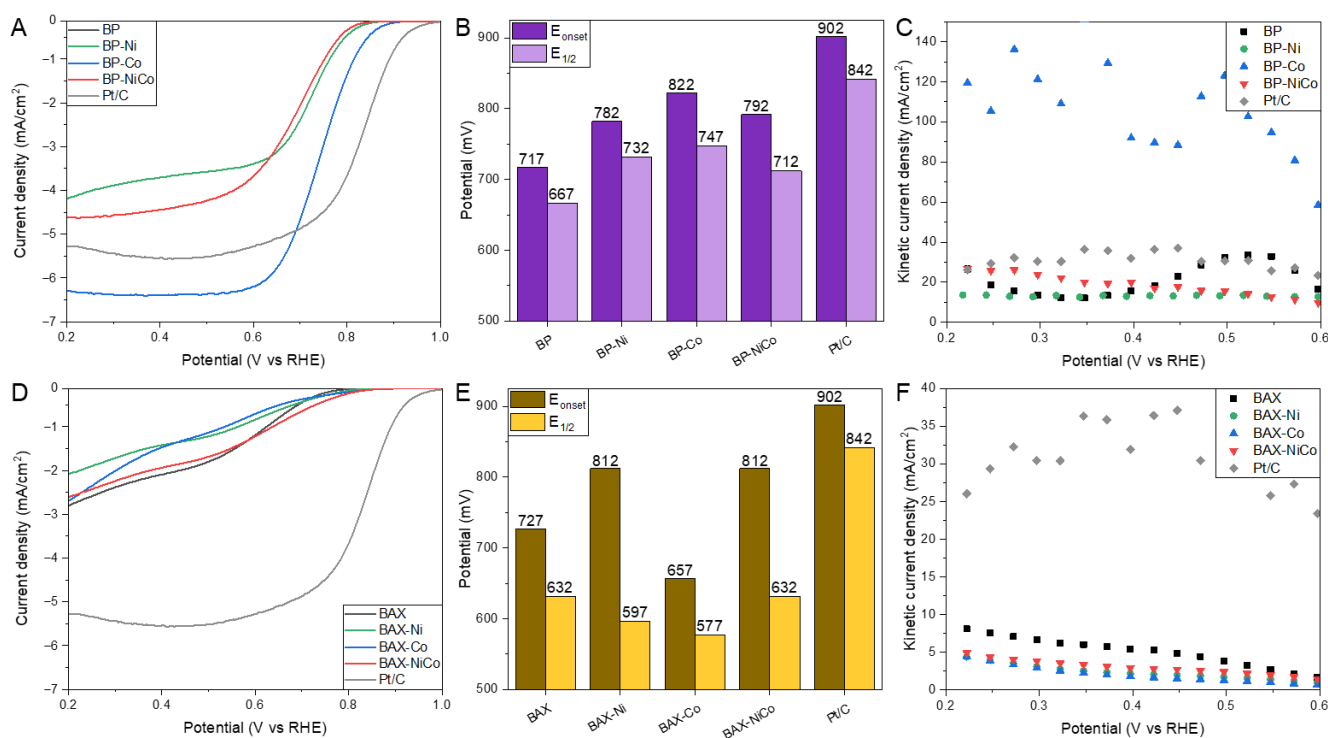


**Figure 2.** Current density for the BP series samples (A) and the BAX ones (D); onset potentials for the BP series samples (B) and the BAX ones (E); the kinetic current densities calculated using Koutecky–Levich Equation for the BP series samples (C) and the BAX one (F).

The LSV curves for the BAX series show marked inferiority in the current density compared to that measured on the BP series (Figure 2D). It is interesting that initially BAX shows the highest current density and highest kinetic current density (Figure 2F), and the modifications with metal have detrimental effects on these quantities. Among the modified samples, Co shows the highest current density; however, it reaches only  $2.6 \text{ mA/cm}^2$ . For this series, the comparison of the onset potential values points to the modification with Ni as the most efficient one and the onset potential on these samples being 90 mV less positive than that on Pt/C (Figure 2E). Nevertheless, the two-wave shape of the LSV curve is still preserved and the current density is low, indicating that even though the process can start at the relatively positive potential value, the ORR process encounters serious limitations on these materials. This low current density led to marked differences between the onset potential calculated using the unbiased SODDM method [76], and the potential

at a half wave. Interestingly, the onset potentials of both initial carbons are quite similar to each other.

The comparison of the number of electrons transferred is presented in Figure 3A,D. Even though for all samples  $n$  values can be considered as reaching 4 (between 3.85 and 4), indicating the high efficiency of the reduction process, in this case the BP series also outperforms the BAX one. Nevertheless, for both series, the best results are obtained on the cobalt-containing samples, and mixing nickel and cobalt (= less cobalt) worsened the performance even when compared to that of the initial samples. Values of  $n$  close to four were reported on many carbon-based samples containing cobalt and modified by various approaches [15,52,81], but it is important to mention that the performance of our modified BP samples is better than that reported by Liu et al. [71] and by Goubert-Renaudin and Wieckowski [68] on the same catalyst support. It is also important to bring up that the amount of peroxide formed on the cobalt-containing samples (Figure 3B,E) is even smaller than that on Pt/C and the highest amount formed on BAX-Ni reaches only 8%, which is significantly lower than on other carbon samples reported with similar number of electrons transferred [81].

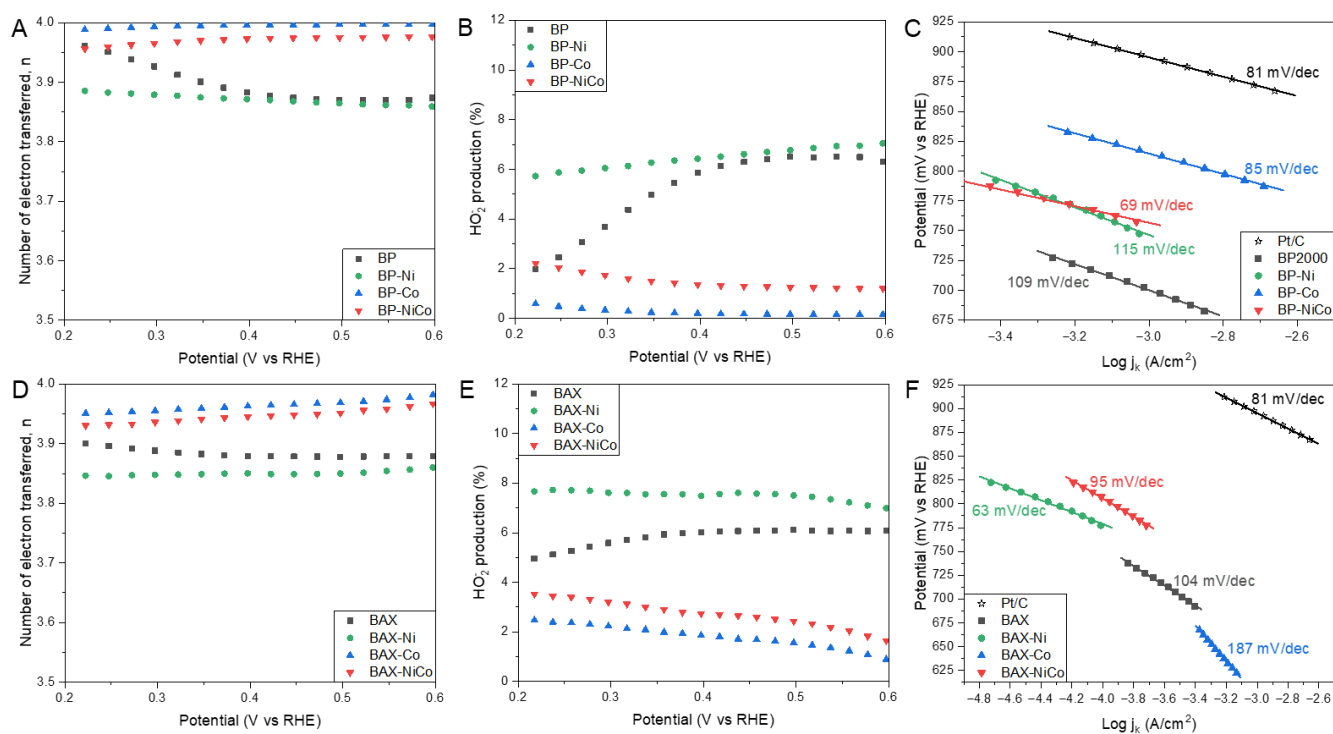


**Figure 3.** The number of electrons transferred on the BP series samples (A) and the BAX ones (D); percent of  $\text{HO}_2^-$  formed in the BP series samples (B) and the BAX ones (E); Tafel plot for the BP series samples (C) and the BAX ones (F).

The Tafel plot slopes' values are linked to the kinetics of an electron transfer [24]. Figure 3C,E,F show the Tafel plots with their calculated slopes. For Pt/C the slope of 0.81 mV/dec was found and BP-Co exhibits a very similar behavior. The modification improves the kinetics of the ORR process on both series of carbons. The worst kinetics are on the BAX series and especially on BAX-Co, and the best, even better than that on Pt/C, are on BAX-Ni. In terms of the kinetics of the electron transfer, modified carbon black tested by Cheng et al. [52] showed better results, which might be attributed to the additional modification of their catalyst support by nitrogen.

The stability of the catalysts is compared in Figure 4A,D. While all BAX samples are less stable than is Pt/C, in the case of the BP series, better performance than that of Pt/C was found for the single-metal-modified samples, but their stability is worse than that of the initial BP. Interestingly, in the case of the BAX series, the modification increased the stability

compared to that of the initial sample, which might be linked to exposing carbon to a higher temperature than that used in the synthesis of original BAX (600 °C). The difference between the BP and BAX series are likely caused by the differences in susceptibility of their carbon matrices to oxidation by formed  $H_2O_2$ . Testing of the effect of the methanol cross-over shows the significantly higher stability of all samples tested than that of Pt/C (Figure 4B,E).

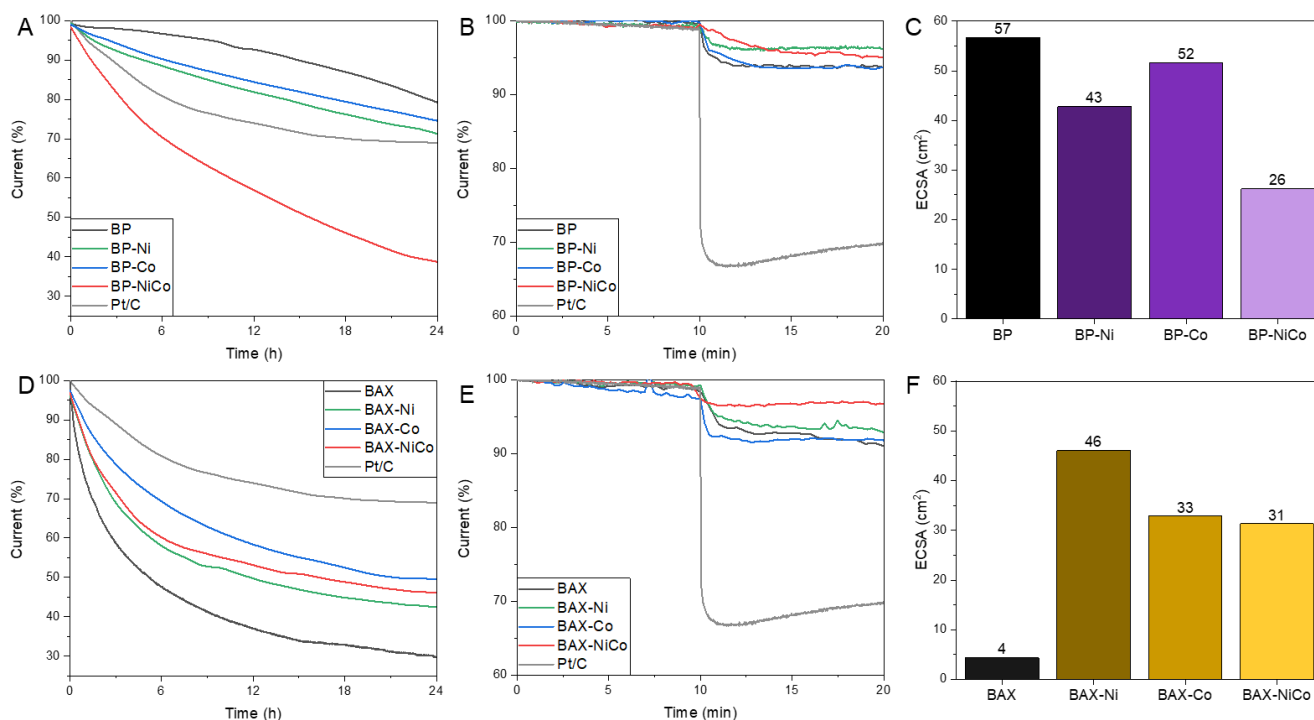


**Figure 4.** Stability of the BP series (A) and of the BAX ones (D); stability to methanol cross-over to the BP series (B) and BAX ones (E). ECSA of the BP (C) and BAX series (F).

The measured ECSA are collected in Figure 4C,F. This parameter is considered as reflecting the specific activity of a catalyst, and the highest values measured for the BP and BAX series are those on BP-Co and BAX-Ni, respectively, which reflects the trend found in the onset potential values. Mixing Ni and Co decreases ECSA, which is also the observed effect on other ORR process descriptors. Interestingly, initial BP has higher ECSA than the modified samples while a totally opposite trend was found for the BAX series. This might indicate that for the initial BP sample, the high electrochemical activity should be linked to totally different factors than those governing the modified BP samples, and those factors were discussed elsewhere [27,30–41]. In the case of the BAX series, the modification with metals introduced highly active in ORR surface sites.

The presented above results of the electrochemical tests clearly show the effects of a carbon support on the performance of the catalysts. This performance is expected to be markedly influenced by resulting chemistry and the porosity of the catalysts influenced by the support. An important factor in our consideration is that the amounts of Ni and Co salts originally used for the modifications and the conditions of the treatments were the same for both series of samples. Therefore, any differences/trends in the surface properties should be linked to the effects of the carbon support and the interactions of their surfaces with deposited Co or/and Ni nitrate salts, and to the complex effects of the applied heat treatment on the resulting surface features. Following the general consensus, a surface rich in carboxylic groups is expected to increase the dispersion of metals, and the thermal decomposition of nitrates into  $NO_x$  might oxidize/activate the surface and cause even some degree of mass loss/volatilization (as CO/ $CO_2$ ) in the case of supports with a low level of carbon ring condensation. It might also result in the development of an additional



porosity. The deposition of salts, especially in large agglomerates, might also block some pores and decrease a pore volume and surface area determined by the  $N_2$  molecule.

To understand the direction of surface chemistry and porosity changes that affect the final catalytic performance, we will first analyze the differences in the nature of the metal species deposited on the carbon surfaces. Even though these carbons were arbitrarily chosen owing to the specific micro/mesoporosity resulting in the high BET surface areas, they still differ significantly in other surface features. Burning carbon samples in air provides the information on the content of an inorganic matter, which in our case is considered to contain in majority nickel and/or cobalt oxides, remaining as a residue at 1000 °C. The comparison of TG and DTG curves measured in air is presented in Figure S2. Based on the preparation procedure, the samples should contain ~17% of metals assuming that released nitrogen oxides did not cause an extensive burn-off of the carbon matrix. This seems to be the case for the BP series where ~20% of metal oxides are detected for all samples. The situation is different for the BAX series, where the content of metal oxide exceeds the theoretical amount and is about 5% higher than in the BP series. A plausible explanation is more extensive burn-off of the BAX support resulting in the removal of carbon as  $CO_2/CO$  during the thermal treatment in nitrogen. Obviously, more metal species on the surface of the BAX series did not lead to the higher catalytic activity.

Some information about the differences in chemistry of the metal species can be provided by the thermal analysis conducted in argon, and the results, as TG and DTG curves, are presented in Figures 5A,B and S3, respectively. Thermal events related to the decomposition and reduction of surface species by carbon are seen as weight losses on the TG curves or peaks on the DTG curves. Compared to the initial BP sample, the modified samples of this series exhibit a very chemically heterogeneous surface (Figure 5A). The first weight loss between 200 and 300 °C is linked to the dehydroxylation of either  $Co(OH)_2$  or  $Ni(OH)_2$ , which leads to the formation of corresponding oxides that are reduced to metal between 500 and 700 °C. This process is reflected by sharp decreases in the weight. In the case of BP-Co, two steps are visible in this temperature range, suggesting the presence of cobalt in a higher oxidation state than +2, which was first reduced to CoO and then the reduction of the latter took place. The weight loss pattern for BP-Co suggests that hydroxide is present in a very small amount, or the particles of cobalt oxides are rather small and their reduction takes place gradually between 300 and 600 °C, with larger particles reduced at higher temperatures. The shape of the TG curve for BP-Ni rather suggests the less heterogeneous distribution of sizes than that for BP-Co, since a well-defined reduction event is detected at ~400 °C. The weight loss of BP-NiCo is apparently influenced by some mixed Co/Ni forms. For the BAX series, the comparison of the weight loss pattern of the modified samples with that of the initial sample should be performed only up to 600 °C, since it is the highest temperature that carbon was exposed to during its production. Gradual weight losses for BAX-Ni and BAX-NiCo suggest the presence of oxygen-containing particles of various sizes. The BAX carbon matrix reduces the majority of oxides between 500 and 800 °C and a two-step weight loss in this temperature range implies that some Co might be in a +3 oxidation state. In fact, the weight loss for BAX-Ni, and especially that for BAX-Co, resemble that for BP-Co between 600 and 800 °C; however, the reduction of the former sample starts to occur at lower temperatures, ~500 °C. The results of the thermal analysis in argon suggest that the particles of metal species/oxides on BP are larger than those on BAX, especially in the case of cobalt, and the particle sizes in the case of BAX are more heterogeneous in their sizes' range.

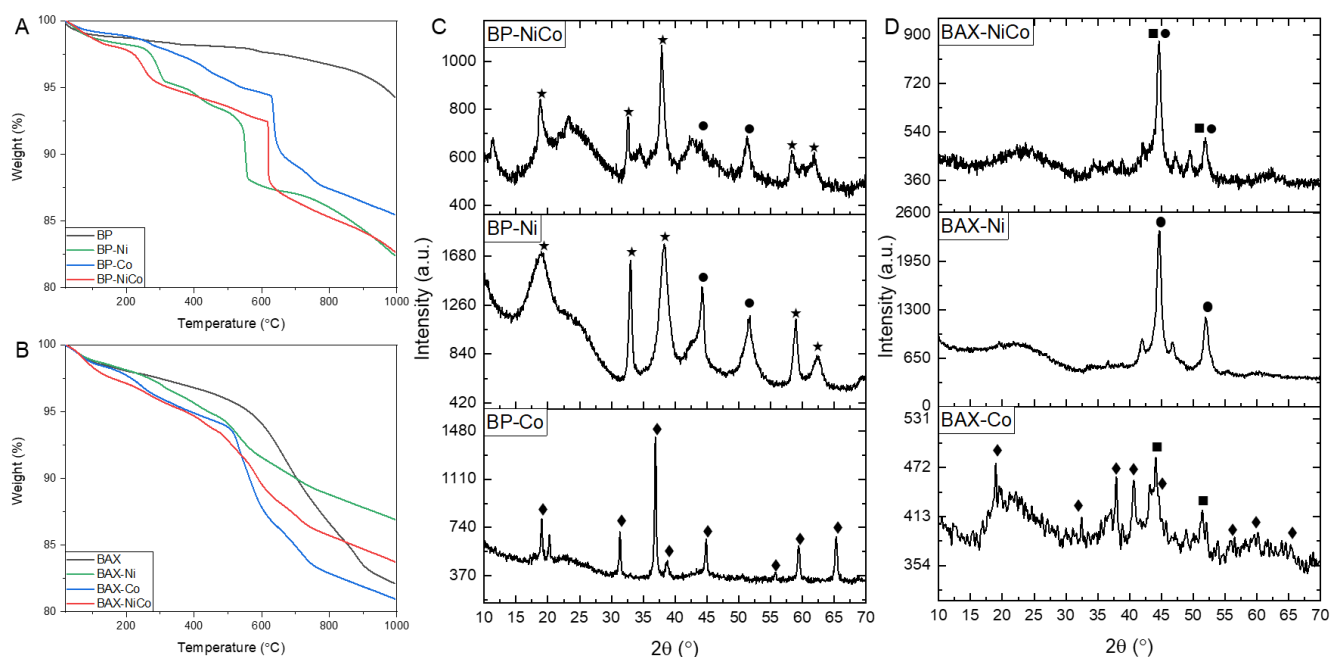


**Figure 5.** TG curves in argon for the BP series (A) and the BAX ones (B); XRD of the BP series (C) and the BAX ones (D); ■, ● Co and Ni cubic Fm-3 m, respectively, ★ Ni(OH)<sub>2</sub> hexagonal P-3m1, ◆ Co<sub>3</sub>O<sub>4</sub> cubic Fd-3 m.

X-ray diffraction experiments bring information about the speciation of the crystallographic phases and on the sizes of the crystals on the surface of the carbon supports (Figure 5C,D). For the BP series, the highest crystallinity level of the deposited species is seen for BP-Co, whose diffractogram shows many sharp peaks representing Co<sub>3</sub>O<sub>4</sub> with large crystals sizes of 27.5 nm, as calculated from the Scherrer Equation. The BP-Ni crystallographic phases are more chemically heterogeneous and broader than in the case of BP-Co diffraction peaks, and are assigned to Ni(OH)<sub>2</sub> and metallic nickel crystals with sizes of about 6.2 and 6.9 nm, respectively. The presence of hydroxide in the case of BP-Ni is consistent with the sharp weight loss seen at ~300 °C on the TG curve of this sample measured in argon (Figure 5A). When Ni and Co are deposited simultaneously on the surface of the BP sample, the resulting crystallographic phases are the same as in the case of BP-Ni but the sizes of crystals are slightly larger, where Ni(OH)<sub>2</sub> size is ~12.2 and that of Ni metal particles of 10.4 nm.

The diffraction patterns of the BAX series totally differ from those of the BP samples. Even though some crystals are present on the surfaces, the results suggest that the inorganic species are more dispersed than are in the latter series, and various phases of hydroxides and oxyhydroxides were identified [82], especially on BAX-Co and BAX-NiCo. Their presence might explain a gradual reduction of the surface seen on the TG curves measured in argon (Figure 5B). On both BAX-Co and BAX-Ni, corresponding metal particles are detected with sizes of 5.2 nm and 11.5 nm, respectively. These crystals are also present in BAX-NiCo and their sizes are about 14.6 nm. On BP-Co small crystals of Co<sub>3</sub>O<sub>4</sub> exist. The most dispersed/amorphous inorganic species are on BAX-Ni.

The trends obtained from the TA and X-ray analyses are confirmed in the TEM images of the samples presented in Figure 6, where the metal-containing particles on the surface of the BAX series are much smaller than those on BP, and their dispersion is much higher on the former samples. In the case of the BP series, the highest dispersion of the metal-containing species was found on BP-Ni, and this is consistent with the differences in the diffraction patterns (Figure 5D). These results are confirmed by the EDX maps (Figure 7). The comparison of cobalt and oxygen signals supports the existence of the metal nanoparticles on both BP-Co and BAX-Co. In the case of BP-NiCo, even though there is a strong

indication of the coexistence of both metals in Co+ Ni +O configurations, the analysis of the maps still suggests that the particles of both metals are deposited on the carbon surface.

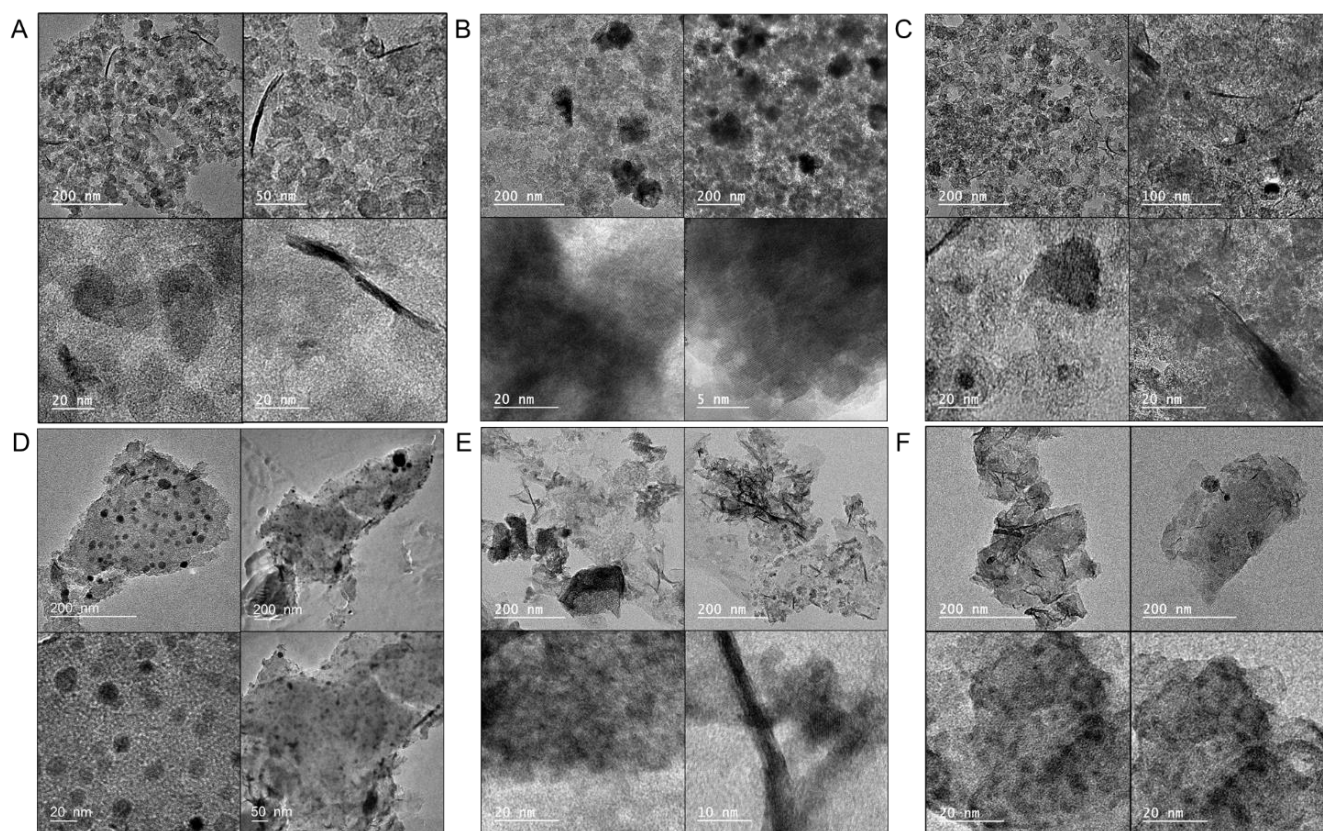


**Figure 6.** TEM images of BP-Ni (A); BP-Co (B); BP-NiCo (C); BAX-Ni (D); BAX-Co (E); and BAX-NiCo (F).

To assess the surface chemical environment in more detail, an XPS analysis was performed and the results are collected in Figures 8 and 9, and in Table S1 of the Supplementary Information. Even though both initial samples have similar contents of oxygen, the thermal treatment with nitrates led to a marked increase in the surface oxygen for the BAX series and to a decrease for the BP series, which might be associated with differences in the oxidation states of both metals, those of the carbon matrices, and the sizes of the oxygen-containing particles. The deconvolution of O 1s core energy level spectra indicates that the vast majority of oxygen in BAX is in oxides with some contributions from hydroxides and carbon–oxygen bonds, while for the BP series oxygen is mainly associated with the metal phase and in the form of hydroxides. The small detected amount of oxygen in the BP series might be linked to the presence of the metal particles or to the existence of the large particles of the oxygen-containing inorganic phase.

As for oxygen, the BAX series also exhibits much more Ni and Co on the surface than does the BP series. As mentioned above, this is likely related to the larger particles of the metal species in the case of BP series. A 7 nm limit of the XPS surface analysis is not able to account for all metals and oxygen present in these particles, leading to their underestimated amounts. Ni 2p<sub>3/2</sub> and Co 2p<sub>3/2</sub> core energy levels were deconvoluted using multiplets based on the deconvolution approach of Biesinger et al. [83]. A combination of Ni, Ni(OH)<sub>2</sub> and NiO was used to deconvolute Ni 2p<sub>3/2</sub>, and a combination of Co, Co(OH)<sub>2</sub>, and Co<sub>3</sub>O<sub>4</sub> was used to deconvolute Co 2p<sub>3/2</sub>, keeping their relative positions, FWHM, and area ratios (as given in Ref. [83]) fixed. Consistently with the X-ray analysis, both Ni and Co metallic particles are clearly detected on the surfaces of BP-Ni and BP-NiCo. While on the BAX carbon sample modified with either Ni or Co and on corresponding BP the metallic particles



are present, on BP-Co mainly  $\text{Co}_3\text{O}_4$  is detected by XPS, in agreement with the X-ray results. Some small contribution of  $\text{Co}(\text{OH})_2$  is also detected and it explains the lack of well-defined weight loss on the BP-Co TG curve associated with dehydroxylation and two well-defined steps associated with the reduction of oxides. The chemical distributions of Ni on the BP and BAX samples are similar, but those of cobalt markedly differ between the series and BAX-Co, BAX-NiCo, and BP-NiCo have more  $\text{Co}(\text{OH})_2$  than  $\text{Co}_3\text{O}_4$ , making BP-Co an outlier in terms of the  $\text{Co}_3\text{O}_4$  content. On both BP-NiCo and BAX-NiCo hydroxides are in the predominant amounts. It is important to mention that on the BP samples nitrogen is detected in about 1 at.% and upon the treatment, its distribution changes and more nitrogen becomes incorporated to the aromatic rings, especially in the case of BP-Co. Regarding the carbon content on the surface, an increase in the detected relative content of carbon on BP can be explained by the presence of the discussed-above large particles of the metal species. Nevertheless, an increase in the contribution of carbon–oxygen bonds in the case of BAX supports mentioned-above oxidation and burn-off of the BAX carbon matrix by released  $\text{NO}_x$ .

Owing to the similarity in preparation, the discussed-above differences in the chemistry of the deposited metal species and in their distribution on the surfaces are expected to be mainly governed by the chemical features of the carbon matrices, which were discussed in detail elsewhere [84]. Here, for the sake of comparison, we reintroduce important information on carbon surface pH, the nature of oxygen groups, and density of those group on the surface of mesopores, where dissociating groups are expected to exist. These features are anticipated to affect chemistry most. Even though both carbons are micro/mesoporous (Table 1), the surface in mesopores composes 38% of the total surface area for BAX and 26% for BP. Taking into account that on the surface of BAX and BP 1.42 and 0.41 mmol/g of dissociating groups are present (0.71 and 0.19 mmol/g of carboxylic groups), respectively, there are much more groups per unit surface area in the case of BAX than BP (an order of magnitude difference in an average density). Thus, these groups increase the dispersion of the metal cations via cation exchange process and polar interactions. With the same amounts of nitrates needed to be distributed through the surfaces, or even more in the case of the modified BAX samples, this difference leads to the higher density of the metal species and their smaller sizes on the surface of BAX than on BP. This is in agreement with the results of the thermal analysis, XRD, and XPS discussed above. The small sizes of the deposited nitrate particles are readily reduced by the carbon surface during the preparation heat treatment up to 850 °C, forming the metal nanoparticles on the BAX sample. They might even coalesce due to the surface oxidation/decomposition of oxygen groups, forming the well-defined crystals. The relatively large particles of  $\text{Co}_3\text{O}_4$  visible on the surface of BP-Co are formed by oxidation of CoO in large “islands”, existing due to the scarcity of oxygen-containing dissociating group, by  $\text{NO}_x$  from the decomposition of nitrates. The metal contents in the BP series suggest that burn-off/activation of the surface during the preparation heat treatment occurred to a rather small extent. Highly dispersed  $\text{Co}(\text{OH})_2$  formed on the functional groups remains on the surface, as a result of the contact of CoO with ambient air/moisture. In the case of BP-Ni, NiO from the decomposition of nitrates cannot undergo oxidation and remain on the surface in its original form or as  $\text{Ni}(\text{OH})_2$ . Here, the highly dispersed small particles of the nickel species are reduced to nickel metal. This is because  $\text{NO}_x$  is able to oxidize only carbon, and formed carbon monoxide is a reducing agent to NiO. In the case of BAX, generally much smaller particles of nitrates were deposited on the surface and therefore the crystallographic phases are not well-defined. Here,  $\text{Co}_3\text{O}_4$  is formed in a much smaller extent not only due the acidic nature of that carbon (pH of BAX is 4.73 vs. 7.98 of BP [84]) but also due to the preference of  $\text{NO}_x$  to oxidize the carbon matrix, as indicated by the TA analysis in air. Interestingly, the surfaces of BP and BAX led to the same extent of the contributions of nickel species, although the  $\text{Ni}(\text{OH})_2$  and NiO particles are much smaller on the surface of BAX and the metal particles are smaller on BP. In the case of mixed metal samples, nickel is present mainly as hydroxides, as also detected by X-ray diffraction. Cobalt is also in majority as

$\text{Co(OH)}_2$ ; however, it exists in a highly dispersed form. The small particles of  $\text{Co}_3\text{O}_4$  are also present and their contribution is slightly higher on BAX-NiCo than on BP-NiCo.

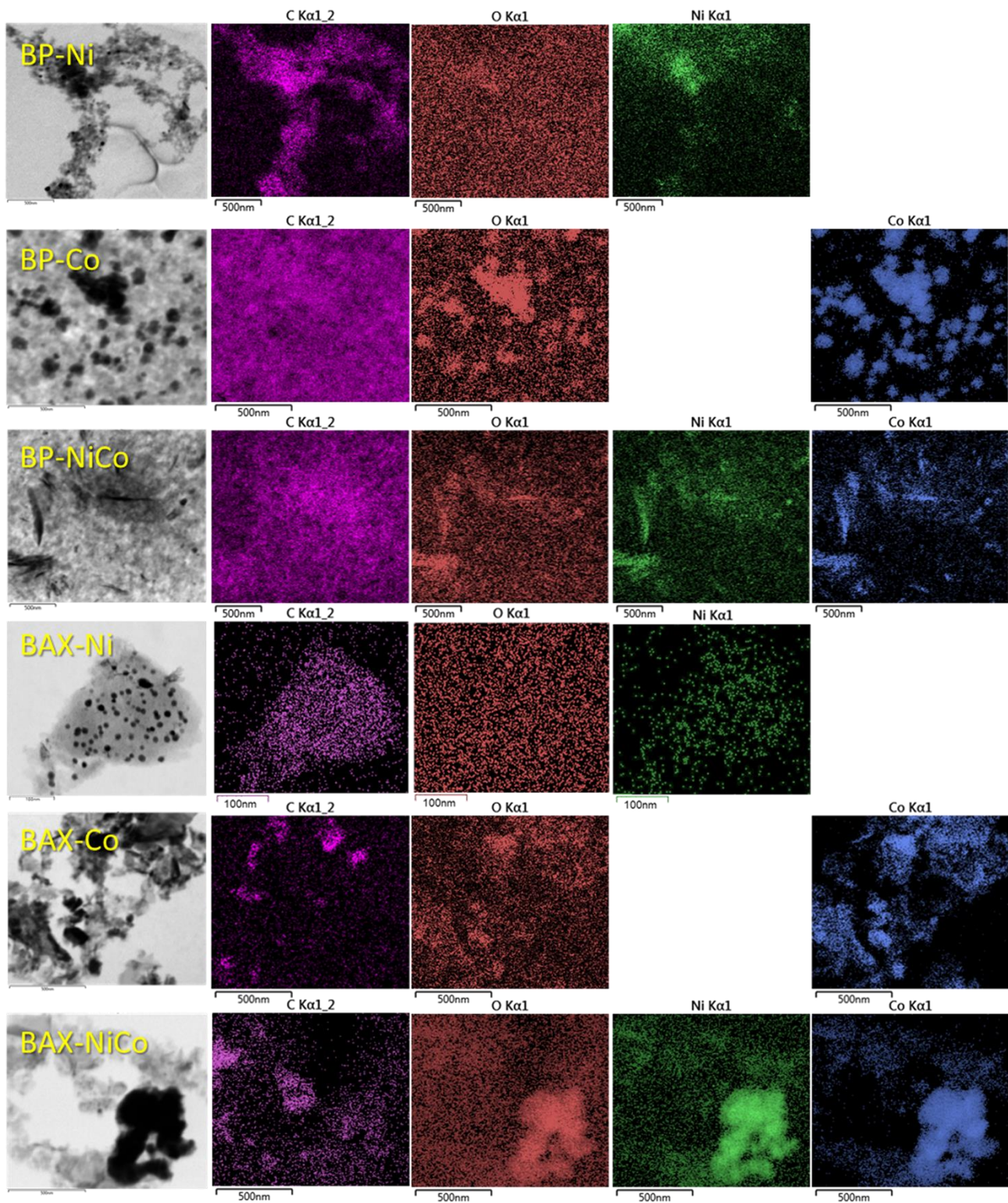


**Figure 7.** EDX maps of the BP and BAX series of samples.



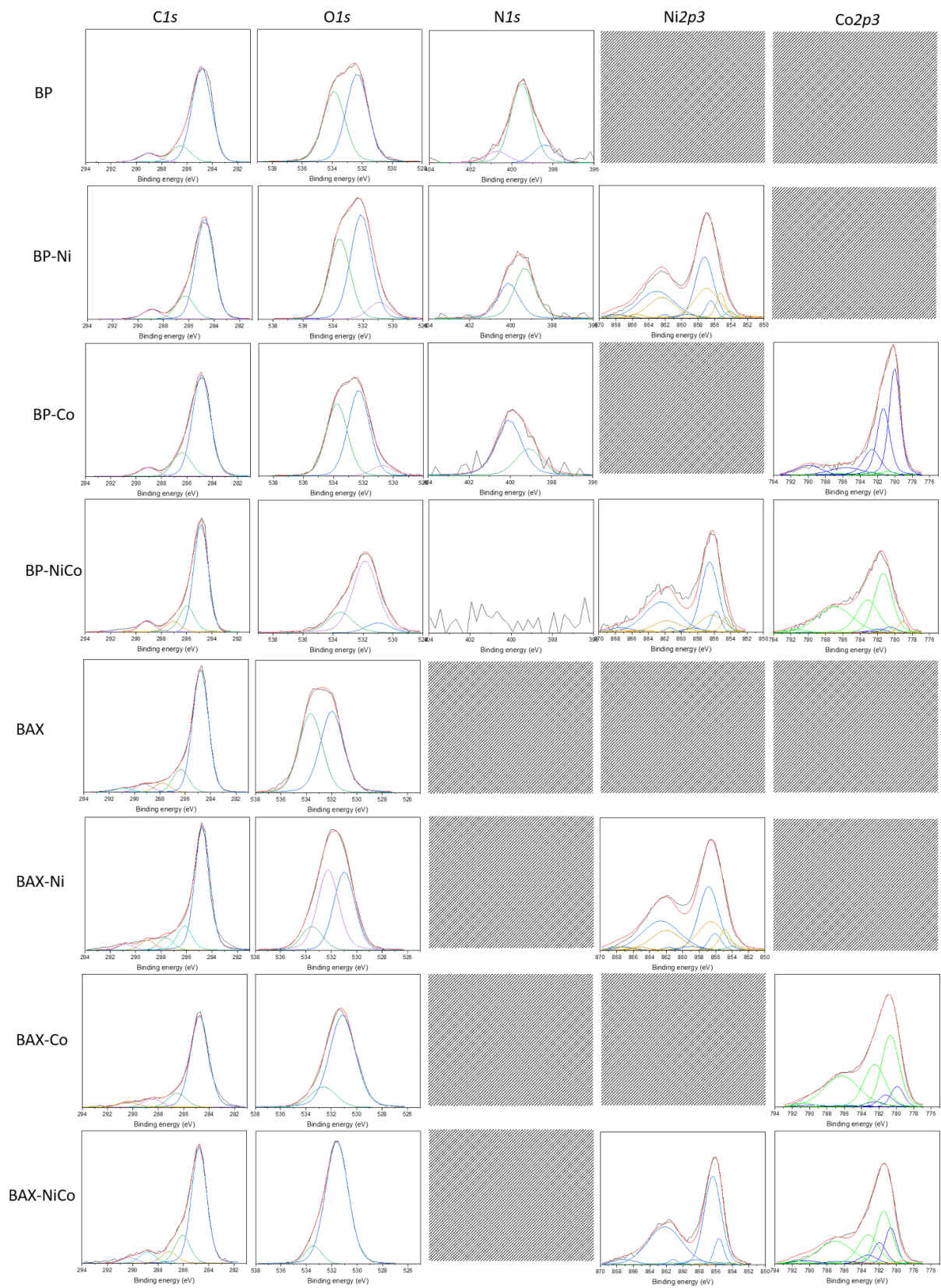


**Figure 8.** Deconvoluted C 1s, O 1s, N 1s, Co 2p and Ni 2p core energy level spectra (the lines of different colors are used for better visibility of the spectra components).

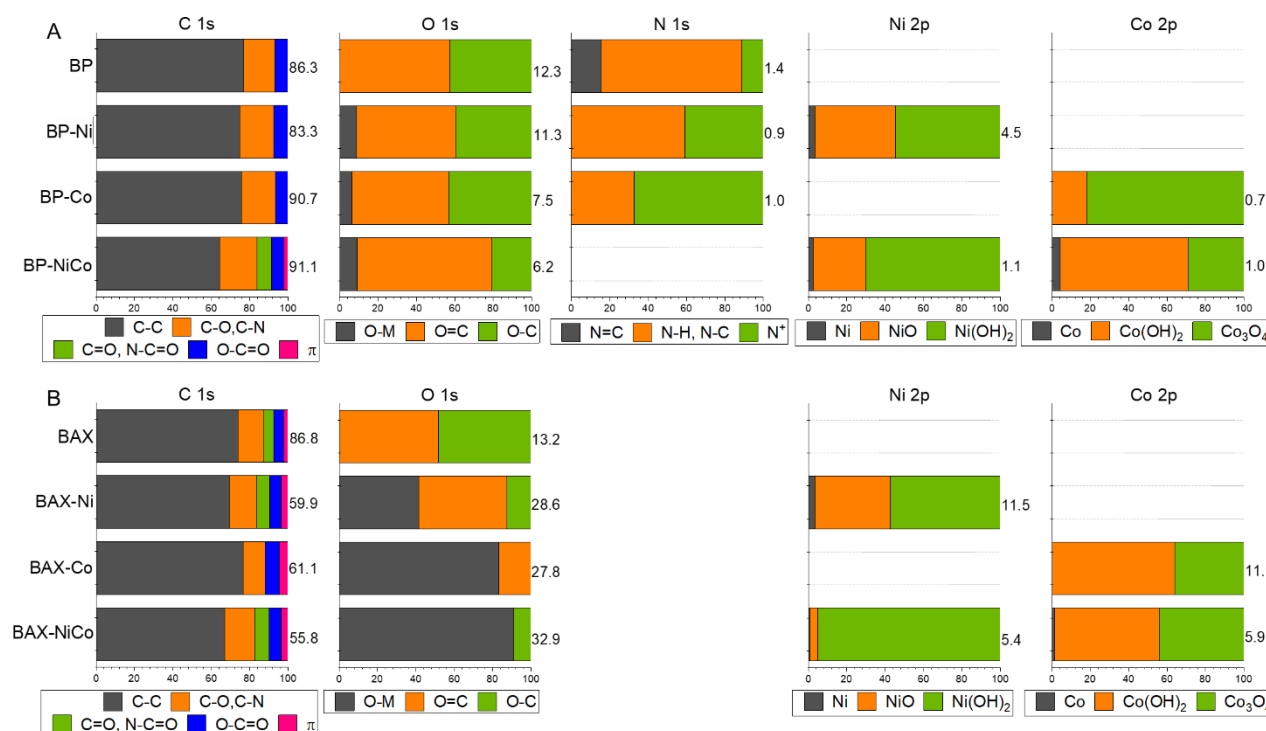


**Figure 9.** Atomic % of the elements on the surface (as numbers on the right of each segment) and the contributions of various bonds from the deconvolution of C 1s, O 1s, N 1s and S 2p core energy level spectra (in % contribution on x axes (from 1–100 %) for the BP series (A) and BAX series (B)).

**Table 1.** The parameters of pore structure.

Samples	$S_{\text{BET}}$ $\text{m}^2/\text{g}$	$V_{\text{tot}}$ $\text{cm}^3/\text{g}$	$V_{<0.7}$ $\text{cm}^3/\text{g}$	$V_{\text{mic}}$ $\text{cm}^3/\text{g}$	$V_{\text{mes}}$ $\text{cm}^3/\text{g}$	$V_{\text{mes}}/V_{\text{tot}}$ %
BP	1609	2.705	0.001	0.532	2.173	80
BP-Ni	1201	1.919	0.063	0.361	1.558	81
BP-Co	1295	2.141	0.066	0.388	1.753	82
BP-NiCo	1161	1.889	0.067	0.356	1.533	81
BAX	2158	1.424	0.079	0.725	0.699	49
BAX-Ni	741	0.436	0.141	0.321	0.115	26
BAX-Co	658	0.425	0.113	0.272	0.153	36
BAX-NiCo	724	0.451	0.119	0.294	0.157	35

$S_{\text{BET}}$ —surface area,  $V_{\text{tot}}$ —total pore volume,  $V_{<0.7}$ —volume of ultramicropores,  $V_{\text{mic}}$ —volume of micropores,  $V_{\text{mes}}$ —volume of mesopores and  $V_{\text{mes}}/V_{\text{tot}}$ —mesoporosity degree.

The analysis of porosity of the materials tested might bring information not only on the dispersion of the metal phase and on the accessibility of the pores for the electrolyte with dissolved oxygen, but also on the activation/burn off processes taking place during the sample preparation, as speculated above. The measured nitrogen adsorption isotherms and calculated from them pore size distributions and presented in Figure 10A,D. The calculated parameters of the pore structure are collected in Table 1. While the amounts of  $\text{N}_2$  adsorbed on the modified BP samples decreased only slightly compared to that on the initial sample, for the BAX samples a significant decrease in the nitrogen uptake was found. As seen in Table 1, the surface area of modified BAX decreased almost three-fold compared to that of the initial sample. A marked increase in the volume of ultramicropores ( $V_{<0.7}$ ) supports surface activation by  $\text{NO}_x$ . On the other hand, over a 50% decrease in the volume of micropores indicates that the deposited species blocks an access of the probe nitrogen molecule to the small pores. The biggest decrease was found in the volume of mesopores and it might be caused by the deposition of the metal species on their surface

functional groups, decreasing mesopore sizes markedly. The increase in the volume of ultramicropores is greater for BAX-Ni than that for BAX-Co, which supports the strong oxidation effects of  $\text{NO}_x$  on the carbon matrix of BAX-Ni, as compared to that on the latter sample. In the case of BP samples the porosity of the modified samples is similar, although the nickel-containing sample still exhibits a slightly greater decrease in the surface area compared to that of BP-Co. In these samples some ultramicropores were formed, which could be due to the deposit of relatively large inorganic particles in supermicropores and in mesopores, causing a decrease in their sizes. Moreover, some slight effects of activation by  $\text{NO}_x$  cannot be crossed out.

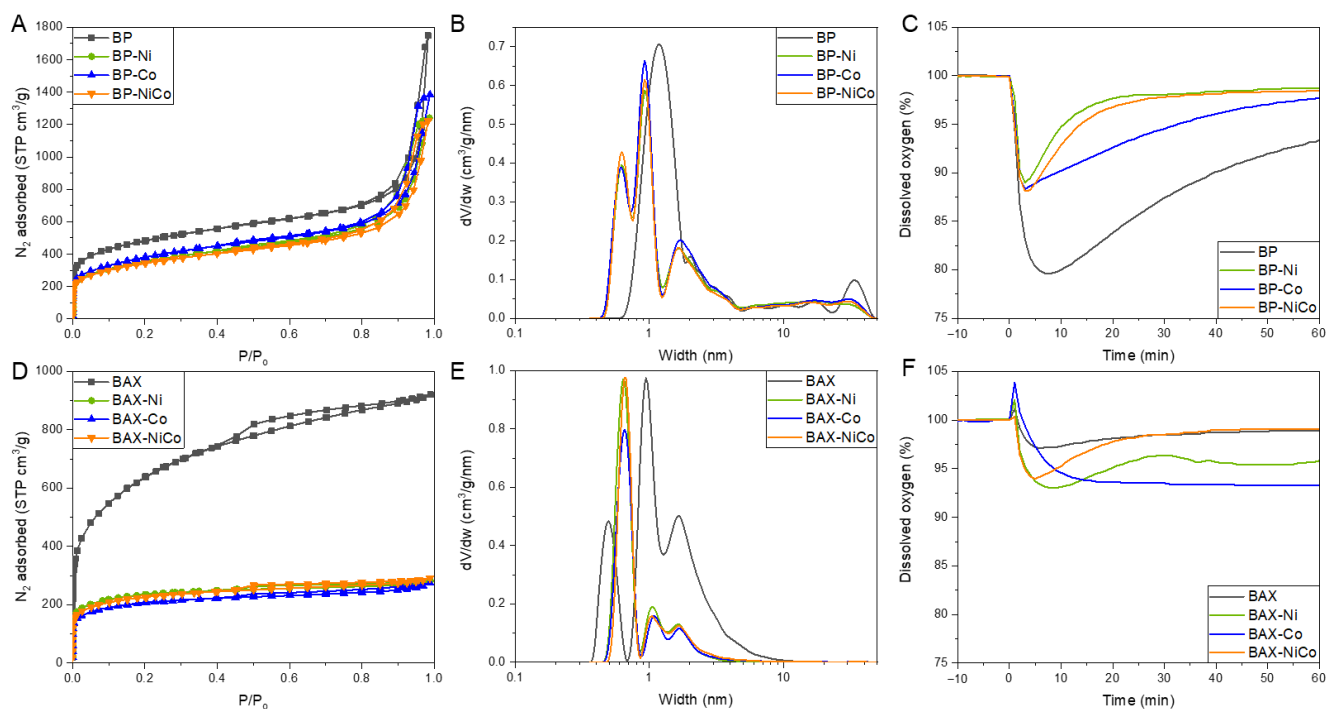


**Figure 10.**  $\text{N}_2$  adsorption isotherms for the BP series (A) and the BAX ones (D); pore size distributions for the BP series (B) and the BAX ones (E); adsorption of oxygen from solution on the BP series (C) and the BAX ones (F).

The pore size distributions presented in Figure 10B,E show the narrowing of the small pores in the BP samples upon the modifications, with a bimodal distribution in the range of micropores. Large mesopores of the BP sample with sizes of about 30 nm significantly decreased in their volume. BAX carbons, although micro/mesopores, have sizes of mesopores reaching only 10 nm and this spatial constraint can be responsible for a marked decrease in their sizes due to the deposition of the inorganic species. For this carbon the ultramicropores increased in size with a marked increase in their volume. Overall, the resulting sizes of ultramicropores are much smaller in the case of the BP samples, and they might favor oxygen adsorption. A large volume of mesopores with the inorganic particles of polar nature promote the transport of the electrolyte with dissolved oxygen to the catalytic centers located on the surface/in small pores.

Another factor to consider as affecting the efficiency of the ORR process is the conductivity of the samples which significantly differs between the two categories of carbons tested. The BP series is much more conductive than the BAX series (measured resistivity for BP, BP-Ni, BP-Co, and BP-NiCo is 11  $\Omega$ , 12  $\Omega$ , 10  $\Omega$ , and 10  $\Omega$ , respectively, while that for BAX, BAX-Ni, BAX-Co, and BAX-NiCo is 1.4 M $\Omega$ , 0.2 k $\Omega$ , 0.3 k $\Omega$ , and 9 k $\Omega$ , respectively) and this certainly is related to the level of carbon aromatization/graphitization and the nature/amount of oxygen groups. The increased graphitization level of the carbon matrix by the heat treatment at 850  $^\circ\text{C}$  combined with the deposition of the metallic particles might

explain an increase in the conductivity of BAX-Ni and BAX-Co, which positively affects the performance of these catalysts.

The trend in oxygen adsorption from its saturated solution upon the addition of the catalyst is presented in Figure 10D,F. As expected, based on the distribution of the pore sizes and their volume, there are not marked differences in the maximum of the amount of oxygen adsorbed within series. The BAX samples adsorb less oxygen than do the BP ones, which might contribute to their overall lower catalytic activity [41], and which is in agreement with the differences in the volume and sizes of ultramicropores. Interestingly, the differences are seen in the kinetics of the process where BP-Co and BAX-Co show prolonged adsorption of O<sub>2</sub> upon its time-dependent dissolution in water. This might be related to the small sizes of cobalt Co<sup>+2</sup> particles (other than Co<sub>3</sub>O<sub>4</sub>) on these samples, which might be undergoing oxidation to Co<sub>3</sub>O<sub>4</sub>, and those in situ formed catalytic centers (also during the ORR process) might be responsible for the higher stability of these samples compared to their Ni-containing and BP-based counterparts.

The analysis of the differences in the surface features of our samples that are indicated in the literature as important to ORR, and discussed above, allow us to provide a plausible explanation of not only the good catalytic activity of the BP series and especially that of BP-Co, but also to suggest the surface features of the BAX series which result in its inferior behavior. The conductivity of the BP series is certainly their important asset, elevating the current compared to that on the BAX series. Another important feature of the BP series is the presence of nitrogen on the surface. Even in small amounts, that nitrogen, when incorporated to the carbon rings was indicated as enhancing ORR [12,17,19,20,28,34,35,38,42,52,72]. The XPS results showed that the thermal treatment in the presence of metallic species increased the contribution of this specific nitrogen, and thus a nitrogen coordination to metals and the creation of single metal catalytic centers cannot be crossed out [77,78,81]. The BP series have also much smaller ultramicropores than those in the BAX series and this factor is expected to contribute to ORR via strong adsorption of oxygen, followed by its bond splitting [27,34–41]. Additionally, this factor might also contribute to the better performance of the initial BAX carbon than some of its modified counterparts, owing to its much higher porosity. A support for the role of micropores is also the larger number of electrons transferred for all BP samples than those for BAX.

Nevertheless, among the BP samples marked differences in the performance still exist, and BP-Co has been found to be the best catalyst, with the current density higher than that on Pt/C. Since the porosities and conductivities of the BP series are similar to each other, that effect can only be linked to the chemistry of the metal species deposited on the surfaces, in addition to the presence of those hypothesized above catalytic centers based on metal–nitrogen bonds. Since the analyses indicated that Co<sub>3</sub>O<sub>4</sub> is the predominant species on the surface of BP-Co, we link the excellent performance of this sample to these species, which were also reported in the literature as catalytically active [52,57]. Support for the hypothesized effect of single metal atoms in coordination with nitrogen is the second-best performance of BP-Ni, and these N-M coordinated metals are also expected in the case of nickel modification. The highly dispersed metal particles might also bring the catalytic activity to the Ni-containing samples [85].

As also observed for the BP series, the BAX samples do not differ markedly in the porosity, and the difference in the performance between the samples in this series is expected to be predominantly governed by their surface chemistry. Here, the performance of both nickel-containing samples, BAX-Ni and BAX-NiCo, in terms of the onset potential is similar to that of the BP series, and taking into account all other features of these samples bringing catalytic disadvantages, this suggests that for this quantity the chemistry of the catalytic species is a predominant factor. In addition, the results imply here that the predominant feature governing the onset potential could be highly dispersed nickel and cobalt metal nanoparticles [59,83]. Moreover, the overall performance of BAX-NiCo in terms of the onset potential is better than that of BP-NiCo owing to its higher content of the Co<sub>3</sub>O<sub>4</sub> catalyst; however, on this carbon the catalytic action of these species is inhibited owing



to overpowering effects of other factors contributing negatively to the efficiency of these series of carbons. The catalytic activity of  $\text{Co}_3\text{O}_4$  has been previously linked to the coupling between the carbon surface and this species [86]. Moreover, the specific facets of the crystals might also play a role, as indicated by Liu et al. [87] based on the DFT calculations of the  $\text{Co}_3\text{O}_4$  activity in an acidic electrolyte.

#### 4. Conclusions

The results collected show the significant effect of carbon matrix properties on the surface features of the catalysts, and thus on the catalytic performance of Ni- and/or Co-modified carbons influenced by them. The exact same modification procedure resulted in differences in the chemistries of the deposited species, in the sizes of the particles, and in the porosity of the materials. A more oxidized carbon surface, owing to the high density of oxygen groups attracting metal salts during impregnation, led to the high dispersion of metal species of small particle sizes, and thus promoted the formation of metal nanoparticles thorough reduction process, especially in the case of the modification with nickel, where the metal particles were found as promoting ORR. When cobalt was used as a modifier,  $\text{Co}_3\text{O}_4$  was formed and it provided excellent catalytic activity, especially for the BP carbon sample whose surface was poor in dissociating groups. In that case an oxidizing action of  $\text{NO}_x$  was directed mainly to oxidize cobalt and to form spinel  $\text{Co}_3\text{O}_4$ . The ORR catalytic efficiency of highly porous carbon black modified with cobalt was only inferior to Pt/C in the slightly lower onset potential, while the current density was much higher than that on Pt/C and the number of electrons transferred reached four with a high catalytic stability. The excellent performance of that carbon black was also linked to its high electric conductivity and porosity. The latter, by the high volume of ultramicropores, enhanced oxygen adsorption and thus provided a pseudocatalytic action complementing the overall influence of catalytic metal-based sites, and especially that of the  $\text{Co}_3\text{O}_4$  particles. These results show promise in the application of commodity carbon blacks as ORR catalysts.

**Supplementary Materials:** The following supporting information can be downloaded at: <https://www.mdpi.com/article/10.3390/nano12244432/s1>, Figure S1: Ring and disk currents at different rotation (0–2000rpm) of the different samples: BP (A), BP-Ni (B), BP-Co (C), BP-NiCo (D), BAX (E), BAX-Ni (F), BAX-Co (G) and BAX-NiCo (H); Figure S2: TG (A,C) and DTG (B,D) curves measured in air of the BP series (A,B) and of the BAX series (C,D); Figure S3: DTG curves measured in argon of the BP series (A) and of the BAX series (B); Table S1: the atomic content of elements on the surface (in bold) and the deconvolution results of collected core energy level spectra.

**Author Contributions:** M.F.: conceptualization, methodology, validation, investigation, data curation, writing—review and editing, visualization. T.J.B.: conceptualization, methodology, validation, resources, writing—original draft preparation, writing—review and editing. All authors have read and agreed to the published version of the manuscript.

**Funding:** This research was partially funded by PSC-CUNY grant number 63556-0051.

**Data Availability Statement:** Raw data available upon request.

**Conflicts of Interest:** The authors declare no conflict of interest.

#### References

1. Sui, S.; Wang, X.; Zhou, X.; Su, Y.; Riffat, S.; Liu, C.-J. A comprehensive review of Pt electrocatalysts for the oxygen reduction reactions: Nanostructure. Activity, mechanism and carbon support in PEM fuel cells. *J. Mater. Chem. A* **2017**, *5*, 1808–1825. [[CrossRef](#)]
2. Wu, G.; Zelenay, P. Nanostructured nonprecious metal catalysts for oxygen reduction reaction. *Acc. Chem. Res.* **2013**, *46*, 1878–1889. [[CrossRef](#)] [[PubMed](#)]
3. Stamenkovic, V.R.; Mun, B.S.L.; Arenz, M.; Mayrhofer, K.J.J.; Lucas, C.A.; Wang, G.; Ross, P.N.; Markovic, N.M. Trends in electrocatalysis on extended and nanoscale Pt-bimetallic alloy surfaces. *Nat. Mater.* **2007**, *6*, 241–247. [[CrossRef](#)] [[PubMed](#)]
4. Liu, X.; Dai, L. Carbon-based metal-free catalysts. *Nat. Rev. Mater.* **2016**, *1*, 16064. [[CrossRef](#)]
5. Yang, Z.; Nie, H.; Chen, X.A.; Chen, X.; Huang, S. Recent progress in doped carbon nanomaterials as effective cathode catalysts for fuel cell oxygen reduction reaction. *J. Power Sources* **2013**, *236*, 238–249. [[CrossRef](#)]



6. Gong, Y.; Li, M.; Wang, Y. Carbon nitride in energy conversion and storage: Recent advances and future prospects. *ChemSusChem* **2015**, *8*, 931–946. [[CrossRef](#)]
7. Han, J.; Bian, J.; Sun, C. Recent advances in single-atom electrocatalysts for oxygen reduction reaction. *Research* **2020**, *2020*, 9512763. [[CrossRef](#)]
8. Gan, Z.Z.; Sheng, Z.M.; Huang, H.; Dai, X.Y.; Niu, R.L.; Jia, R.P. Highly mesoporous Fe and N Co-doped graphitic catalysts prepared from short-time synthesis of precursor towards highly efficient oxygen reduction. *Sustain. Energy Fuels* **2019**, *3*, 3335–3343. [[CrossRef](#)]
9. Yi, J.D.; Xu, R.; Wu, Q.; Zhang, T.; Zang, K.T.; Luo, J.; Liang, Y.L.; Huang, Y.B.; Cao, R. Atomically dispersed iron-nitrogen active sites within porphyrinic triazine-based frameworks for oxygen reduction reaction in both alkaline and acidic media. *ACS Energy Lett.* **2018**, *3*, 883–889. [[CrossRef](#)]
10. Jorge, A.B.; Jervis, R.; Periasamy, A.P.; Qiao, M.; Feng, J.; Tran, L.N.; Titirici, M.-M. 3D carbon materials for efficient oxygen and hydrogen electrocatalysis. *Adv. Energy Mater.* **2020**, *10*, 1902494. [[CrossRef](#)]
11. Zhang, J.; Xia, Z.; Dai, L. Carbon-based electrocatalysts for advanced energy conversion and storage. *Sci. Adv.* **2015**, *1*, e1500564. [[CrossRef](#)] [[PubMed](#)]
12. Yu, L.; Pan, X.; Cao, X.; Hu, P.; Bao, X. Oxygen reduction reaction mechanism on nitrogen-doped graphene: A density functional theory study. *J. Catal.* **2011**, *282*, 183–190. [[CrossRef](#)]
13. Shao, M.; Chang, Q.; Dodelet, J.-P.; Chenitz, R. Recent advances in electrocatalysts for oxygen reduction reaction. *Chem. Rev.* **2016**, *116*, 3594–3657. [[CrossRef](#)]
14. Ma, R.; Lin, G.; Zhou, Y.; Liu, Q.; Zhang, T.; Shan, G.; Yang, M.; Wang, J. A review of oxygen reduction mechanisms for metal-free carbon-based electrocatalysts. *NPJ Comput. Mater.* **2019**, *5*, 78. [[CrossRef](#)]
15. Chen, L.; Xu, X.; Yang, W.; Jia, J. Recent advances in carbon-based electrocatalysts for oxygen reduction reaction. *Chin. Chem. Lett.* **2020**, *31*, 626–634. [[CrossRef](#)]
16. Yan, X.; Jia, Y.; Yao, X. Defects on carbons for electrocatalytic oxygen reduction. *Chem. Soc. Rev.* **2018**, *47*, 7628–7658. [[CrossRef](#)] [[PubMed](#)]
17. Li, H.; Kang, W.; Wang, L.; Yue, Q.; Xu, S.; Wang, H.; Liu, J. Synthesis of three-dimensional flowerlike nitrogen-doped carbons by a copyrolysis route and the effect of nitrogen species on the electrocatalytic activity in oxygen reduction reaction. *Carbon* **2013**, *54*, 249–257. [[CrossRef](#)]
18. Liang, L.; Zheng, Y.; Chen, J.; Liu, J.; Hulicova-Jurcakova, D.; Jaroniec, M.; Qiao, S.Z. Facile oxygen reduction on a three-dimensionally ordered macroporous graphitic C<sub>3</sub>N<sub>4</sub>/carbon composite electrocatalyst. *Angew. Chem. Int. Ed.* **2012**, *51*, 3892–3896. [[CrossRef](#)]
19. Zhang, C.; Hao, R.; Liao, H.; Hou, Y. Synthesis of amino-functionalized graphene as metal-free catalyst and exploration of the roles of various nitrogen states in oxygen reduction reaction. *Nano Energy* **2013**, *2*, 88–97. [[CrossRef](#)]
20. Gong, K.; Du, F.; Xia, Z.; Durstock, M.; Dai, L. Nitrogen-doped carbon nanotube arrays with high electrocatalytic activity for oxygen reduction. *Science* **2009**, *323*, 760. [[CrossRef](#)]
21. Liang, J.; Jiao, Y.; Jaroniec, M.; Qiao, S.Z. Sulfur and nitrogen dual-doped mesoporous graphene electrocatalyst for oxygen reduction with synergistically enhanced performance. *Angew. Chem. Int. Ed.* **2012**, *51*, 11496–11500. [[CrossRef](#)] [[PubMed](#)]
22. Yang, Z.; Yao, Z.; Li, G.; Fang, G.; Nie, H.; Liu, Z.; Zhou, X.; Chen, X.; Huang, S. Sulfur-doped graphene as an efficient metal-free cathode catalyst for oxygen reduction. *ACS Nano* **2012**, *6*, 205–211. [[CrossRef](#)] [[PubMed](#)]
23. Yang, S.; Zhi, L.; Tang, Z.; Feng, X.; Maier, J.; Müllen, K. Efficient synthesis of heteroatom (N or S)-doped graphene based on ultrathin graphene oxide-porous silica sheets for oxygen reduction reactions. *Adv. Funct. Mater.* **2012**, *22*, 3634–3640. [[CrossRef](#)]
24. Choi, C.H.; Park, S.H.; Woo, S.I. Binary and ternary doping of nitrogen, boron, and phosphorus into carbon for enhancing electrochemical oxygen reduction activity. *ACS Nano* **2012**, *6*, 7084–7091. [[CrossRef](#)] [[PubMed](#)]
25. von Deak, D.; Biddinger, E.J.; Luthman, K.A.; Ozkan, U.S. The effect of phosphorus in nitrogen-containing carbon nanostructures on oxygen reduction in PEM fuel cells. *Carbon* **2010**, *48*, 3637–3639. [[CrossRef](#)]
26. Wang, S.; Zhang, L.; Xia, Z.; Roy, A.; Chang, D.W.; Baek, J.-B.; Dai, L. BCN graphene as efficient metal-free electrocatalyst for the oxygen reduction reaction. *Angew. Chem. Int. Ed.* **2012**, *51*, 4209–4212. [[CrossRef](#)]
27. Florent, M.; Wallace, R.; Bandoz, T.J. Oxygen electroreduction on nanoporous carbons: Textural features vs nitrogen and boron catalytic centers. *ChemCatChem* **2019**, *11*, 851–860. [[CrossRef](#)]
28. Quilez-Bermejo, J.; Morallon, E.; Cazorla Amorós, D. Metal-free heteroatom doped carbon-based catalysts for ORR: A critical assessment about the role of heteroatoms. *Carbon* **2020**, *165*, 434–454. [[CrossRef](#)]
29. Li, D.; Jia, Y.; Chang, G.; Chen, J.; Liu, H.; Wang, J.; Hu, Y.; Xia, Y.; Yang, D.; Yao, X. A defect-driven metal-free electrocatalyst for oxygen reduction in acidic electrolyte. *Chem* **2018**, *4*, 2345–2356. [[CrossRef](#)]
30. Morais, R.G.; Rey-Raap, N.; Figueiredo, J.L.; Pereira, M.F.R. Glucose-derived carbon materials with tailored properties as electrocatalysts for the oxygen reduction reaction. *Beilstein J. Nanotechnol.* **2019**, *10*, 1089–1102. [[CrossRef](#)]
31. Morawa Eblagon, K.; Rey-Raap, N.; Figueiredo, J.L.; Pereira, M.F.R. Relationships between texture, surface chemistry and performance of N-doped carbon xerogels in the oxygen reduction reaction. *Appl. Surf. Sci.* **2021**, *548*, 149242. [[CrossRef](#)]
32. Gabe, A.; Ruiz-Rosas, R.; González-Gaitán, C.; Morallón, E.; Cazorla-Amorós, D. Modeling of oxygen reduction reaction in porous carbon materials in alkaline medium. Effect of microporosity. *J. Power Sources* **2019**, *412*, 451–464. [[CrossRef](#)]

33. Eisenberg, D.; Prinsen, P.; Geels, N.J.; Stroek, W.; Yan, N.; Hua, B.; Kuo, J.-L.; Rothenberg, G. The evolution of hierarchical porosity in self templated nitrogen-doped carbon and its effects on oxygen reduction electrocatalysis. *RCS Adv.* **2016**, *6*, 80398–80407. [[CrossRef](#)]
34. Bandosz, T.J. Exploring the silent aspect of carbon nanopores. *Nanomaterials* **2021**, *11*, 407. [[CrossRef](#)]
35. Bandosz, T.J. Revealing the impact of small pores on oxygen reduction on carbon electrocatalysts: A journey through recent findings. *Carbon* **2022**, *188*, 289–304. [[CrossRef](#)]
36. Seredych, M.; Szczurek, A.; Fierro, V.; Celzard, A.; Bandosz, T.J. Electrochemical reduction of oxygen on hydrophobic ultramicroporous PolyHIPE carbon. *ACS Catal.* **2016**, *6*, 5618–5628. [[CrossRef](#)]
37. Encalada, J.; Savaram, K.; Travlou, N.A.; Li, W.; Li, Q.; Delgado-Sánchez, C.; Fierro, V.; Celzard, A.; He, H.; Bandosz, T.J. Combined effect of porosity and surface chemistry on the electrochemical reduction of oxygen on cellular vitreous carbon foam catalyst. *ACS Catal.* **2017**, *7*, 7466–7478. [[CrossRef](#)]
38. Barrera, D.; Florent, M.; Sapag, K.; Bandosz, T.J. Insight into the mechanism of oxygen reduction reaction on micro/mesoporous carbons: Ultramicropores versus nitrogen-containing catalytic centers in ordered pore structure. *ACS Appl. Energy Mater.* **2019**, *2*, 7412–7424. [[CrossRef](#)]
39. Barrera, D.; Florent, M.; Kulko, M.; Bandosz, T.J. Ultramicropore-influenced mechanism of oxygen electroreduction on metal-free carbon catalysts. *J. Mater. Chem. A* **2019**, *7*, 27110–27123. [[CrossRef](#)]
40. de Falco, G.; Florent, M.; Jagiello, J.; Cheng, Y.; Daemen, L.L.; Ramirez-Cuesta, A.J.; Bandosz, T.J. Alternative view of oxygen reduction on porous carbon electrocatalysts: The substance of complex oxygen-surface interactions. *iScience* **2021**, *24*, 102216. [[CrossRef](#)]
41. de Falco, G.; Florent, M.; Bandosz, T.J. Oxygen adsorption in pores promotes its reduction on metal-free carbon catalysts: A case of carbon blacks. *Carbon* **2022**, *189*, 230–239. [[CrossRef](#)]
42. Singh, S.K.; Takeyasu, K.; Nakamura, J. Active sites and mechanism of oxygen reduction reaction electrocatalysis on nitrogen-doped carbon materials. *Adv. Mater.* **2018**, 1804297. [[CrossRef](#)] [[PubMed](#)]
43. Jiang, Y.; Yang, L.; Sun, T.; Zhao, J.; Lyu, Z.; Zhuo, O.; Wang, X.; Wu, Q.; Ma, J.; Hu, Z. Significant contribution of intrinsic carbon defects to oxygen reduction activity. *ACS Catal.* **2015**, *5*, 6707–6712. [[CrossRef](#)]
44. Wang, J.; Yin, G.; Shao, Y.; Zhang, S.; Wang, Z.; Gao, Y. Effect of carbon black support corrosion on the durability of Pt/C catalyst. *J. Power Sources* **2007**, *171*, 331–339. [[CrossRef](#)]
45. Yang, H.; Ko, Y.; Lee, W.; Zuttel, A.; Kim, W. Nitrogen-doped carbon black supported Pt-M (M=Pt, Fe, Ni) alloy catalysts for oxygen reduction reaction in proton exchange membrane fuel cell. *Mater. Today Energy* **2019**, *13*, 374–381. [[CrossRef](#)]
46. Appleby, A.J.; Marie, J. Kinetics of oxygen reduction on carbon materials in alkaline solution. *Electrochim. Acta* **1979**, *24*, 195–202. [[CrossRef](#)]
47. Fruehwald, H.M.; Ebraldize, I.I.; Melino, P.D.; Zenkina, O.V.; Easton, E.B. Probing the influence of the carbon support on the activity of Fe-N<sub>3</sub>/C model active sites for the oxygen reduction reaction. *J. Electrochem. Soc.* **2020**, *167*, 084520. [[CrossRef](#)]
48. Tarasevich, M.R.; Mazin, P.V.; Kapustina, N.A. Kinetics and mechanism of oxygen electroreduction in acidic and neutral solutions on carbon black XC-72R modified by products of pyrolysis of cobalt 5,10,15,20-tetrakis(4-methoxyphenyl) porphyrin. *Russ. J. Electrochem.* **2011**, *47*, 923. [[CrossRef](#)]
49. Zhutaeva, G.V.; Bogdanovskaya, V.A.; Davydova, E.S.; Kazanskii, L.P.; Tarasevich, M.R. Kinetics and mechanism of oxygen electroreduction on Vulcan XC72R carbon black modified by pyrolysis products of cobalt 5,10,15,20-tetrakis(4-methoxyphenyl) porphyrin in a broad pH interval. *J. Solid State Electrochem.* **2014**, *18*, 1319–1334. [[CrossRef](#)]
50. Oh, J.; Park, S.; Jang, D.; Shin, Y.; Lim, D.; Park, S. Metal-free N-doped carbon black s as excellent electro catalysts for oxygen reduction reactions. *Carbon* **2019**, *45*, 481–487. [[CrossRef](#)]
51. Dong, Y.; Li, J. Tungsten nitride nanocrystals on nitrogen-doped carbon black as efficient electrocatalysts for oxygen reduction reactions. *Chem. Commun.* **2015**, *51*, 572–575. [[CrossRef](#)]
52. Cheng, G.; Liu, G.; Liu, P.; Han, S.; Han, J.; Ye, F.; Song, W.; Lan, B.; Sun, M.; Yu, L. Nitrogen doped Ketjenblack carbon supported Co<sub>3</sub>O<sub>4</sub> nanoparticles as a synergistic electrocatalyst for oxygen reduction reactions. *Frontiers Chem.* **2019**, *7*, 766. [[CrossRef](#)] [[PubMed](#)]
53. Lv, Q.; Si, W.; He, J.; Sun, L.; Zhang, C.; Wand, N.; Yang, Z.; Li, X.; Wang, X.; Deng, W.; et al. Selectively nitrogen-doped carbon materials as superior metal-free catalyst for oxygen reduction. *Nat. Commun.* **2018**, *9*, 3376. [[CrossRef](#)] [[PubMed](#)]
54. Kong, F.; Cui, X.; Huang, Y.; Yao, H.; Chen, Y.; Tian, H.; Meng, G.; Chen, C.; Chang, Z.; Shi, J. N-doped carbon electrocatalysts: Marked ORR activity in acidic media without the contribution from metal sites? *Angew. Chem.* **2022**, *61*, e202116290. [[CrossRef](#)] [[PubMed](#)]
55. Bagotzky, V.S.; Shumilova, N.A.; Samoilov, G.P.; Khrushcheva, E.I. Electrochemical oxygen reduction on nickel electrodes in alkaline solutions—II. *Electrochim. Acta* **1972**, *17*, 1625–1635. [[CrossRef](#)]
56. Bagotzky, V.S.; Shumilova, N.A.; Khrushcheva, E.I. Electrochemical oxygen reduction on oxide catalysts. *Electrochim. Acta* **1976**, *21*, 919–924. [[CrossRef](#)]
57. Ouyang, C.; Ni, B.; Sun, Z.; Zhuang, J.; Xiao, H.; Wang, X. Boosting the ORR performance of modified carbon black via C–O bonds. *Chem. Sci.* **2019**, *10*, 2118–2123. [[CrossRef](#)]
58. Xie, S.; Huang, S.; Wei, W.; Yang, X.; Liu, Y.; Lu, X.; Tong, Y. Chitosan Waste-Derived Co and N Co-doped Carbon Electrocatalyst for Efficient Oxygen Reduction Reaction. *ChemElectroChem* **2015**, *2*, 1806–1812. [[CrossRef](#)]

59. Yuan, X.; Hu, X.-X.; Ding, X.-L.; Kong, H.-C.; Sha, H.-D.; Lin, H.; Wen, W.; Shen, G.; Guo, Z.; Ma, Z.-F.; et al. Effects of cobalt precursor on pyrolyzed carbon-supported cobalt-polypyrrole as electrocatalyst toward oxygen reduction reaction. *Nanoscale Res. Lett.* **2013**, *8*, 478. [[CrossRef](#)]
60. Pan, Y.; Wang, M.; Feng, C.H. A doping-adsorption-pyrolysis strategy for constructing atomically dispersed cobalt sites anchored on a N-doped carbon framework as an efficient bifunctional electrocatalyst for hydrogen evolution and oxygen reduction. *RSC Adv.* **2022**, *12*, 20578. [[CrossRef](#)]
61. Wang, L.; Zhang, J.; Zhen, L.; Yang, J.; Li, Y.; Wan, X.; Liu, X.; Zhang, X.; Yu, R.; Shui, J. Carbon black-supported FM–N–C (FM = Fe, Co, and Ni) single-atom catalysts synthesized by the self-catalysis of oxygen-coordinated ferrous metal atoms. *J. Mater. Chem. A* **2020**, *8*, 13166–13172. [[CrossRef](#)]
62. Morais, R.G.; Rey-Raap, N.; Figueiredo, J.L.; Pereira, M.F.R. Fe, Co, N-doped carbon nanotubes as bifunctional oxygen electrocatalysts. *Appl. Surf. Sci.* **2022**, *572*, 151459. [[CrossRef](#)]
63. Kim, S.; Kato, S.; Ishizaki, T.; Li, O.L.; Kang, J. Transition metal (Fe, Co, Ni) nanoparticles on selective amino-N-doped carbon as high-performance oxygen reduction reaction electrocatalyst. *Nanomaterials* **2019**, *9*, 742. [[CrossRef](#)] [[PubMed](#)]
64. Putra, R.P.; Rachman, I.B.; Horino, H.; Rzeznicka, I.I. Bifunctional catalytic activity of  $\gamma$ -NiOOH toward oxygen reduction and oxygen evolution reactions in alkaline Solutions. *Oxygen* **2022**, *2*, 479–492. [[CrossRef](#)]
65. Ashok, A.; Kumar, A.; Ponraj, J.; Mansour, S.A.; Tarlochan, F. Highly active and stable bi-functional nicoo<sub>2</sub> catalyst for oxygen reduction and oxygen evolution reactions in alkaline medium. *Int. J. Hydrog. Energy* **2019**, *44*, 16603–16614. [[CrossRef](#)]
66. Zhang, H.; Liu, M.; Cheng, W.; Li, Y.; Zhou, W.; Su, H.; Zhao, X.; Yao, P.; Liu, Q. Metallic Ni<sub>3</sub>N quantum dots as a synergistic promoter for NiO nanosheet toward efficient oxygen reduction electrocatalysis. *J. Phys. Chem. C* **2019**, *123*, 8633–8639. [[CrossRef](#)]
67. Abdelwahab, A.; Castelo-Quibén, J.; Vivo-Vilches, J.F.; Pérez-Cadenas, M.; Maldonado-Hódar, F.J.; Carrasco-Marín, F.; Pérez-Cadena, A.F. Electrodes based on carbon aerogels partially graphitized by doping with transition metals for oxygen reduction reaction. *Nanomaterials* **2018**, *8*, 266. [[CrossRef](#)]
68. Goubert-Renaudin, S.N.S.; Wieckowski, A. Ni and/or Co nanoparticles as catalysts for oxygen reduction (ORR) at room temperature. *J. Electroanal. Chem.* **2011**, *652*, 44–51. [[CrossRef](#)]
69. Liu, X.; Park, M.; Kim, M.G.; Gupta, S.; Wu, G.; Choi, J. Integrating NiCo Alloys with their oxides as efficient bifunctional cathode catalysts for rechargeable zinc–air batteries. *Angew. Chem.* **2015**, *54*, 9654–9658. [[CrossRef](#)]
70. Fu, Y.; Yu, H.Y.; Jiang, C.; Zhang, T.H.; Zhan, R.; Li, X.; Li, J.F.; Tian, J.H.; Yang, R. NiCo alloy nanoparticles decorated on N-doped carbon nanofibers as highly active and durable oxygen electrocatalyst. *Adv. Funct. Mater.* **2018**, *28*, 1705094. [[CrossRef](#)]
71. Liu, J.; Jiang, L.; Tang, O.; Wang, E.; Qi, L.; Wang, S.; Sun, G. Amide-functionalized carbon supports for cobalt oxide toward oxygen reduction reaction in Zn–air battery. *Appl. Catal. B* **2014**, *148–149*, 212–220. [[CrossRef](#)]
72. Florent, M.; Hashmi, R.; Badosz, T.J. Extent of carbon surface oxygen affinity and its effects on the activity of metal-free carbon catalysts in oxygen reduction reaction: Interplay of porosity and N-, O- and S-enriched surface chemistry. *Mater. Adv.* **2022**, *23*, 8567–8578. [[CrossRef](#)]
73. Jagiello, J.; Olivier, J.P. Carbon slit pore model incorporating surface energetical heterogeneity and geometrical corrugation. *Adsorption* **2013**, *19*, 777–783. [[CrossRef](#)]
74. Suryanto, B.H.R.; Zhao, C. Surface-oxidized carbon black as a catalyst for the water oxidation and alcohol oxidation reactions. *Chem. Commun.* **2016**, *52*, 6439–6442. [[CrossRef](#)]
75. Zhou, R.; Zheng, Y.; Jaroniec, M.; Qiao, S.-Z. Determination of the electron transfer number for the oxygen reduction reaction: From theory to experiment. *ACS Catalysis* **2016**, *6*, 4720–4728. [[CrossRef](#)]
76. de Falco, G.; Florent, M.; De Rosa, A.; Badosz, T.J. Proposing an unbiased oxygen reduction reaction onset potential determination by using a Savitzky-Golay differentiation procedure. *J. Colloid Interface Sci.* **2021**, *586*, 597–600. [[CrossRef](#)]
77. Elghamry, I.; Alablan, A.S.; Alkhalifah, M.A.; Abdelsalam, M.E. High-performance organometallic catalyst based on nickel porphyrin/carbon fibre for the oxygen reduction reaction. *J. Electrochem. Soc.* **2021**, *168*, 016510. [[CrossRef](#)]
78. Giddaerappa, N.; Shantharaja, M.H.; Lokesh, K.S. Tetraphenolphthalein cobalt (II) phthalocyanine polymer modified with multiwalled carbon nanotubes as an efficient catalyst for the oxygen reduction reaction. *ACS Omega* **2022**, *7*, 14291–14304. [[CrossRef](#)]
79. Zhang, X.; Xu, X.; Yao, S.; Hao, C.; Pan, C.; Xiang, X.; Tian, Z.Q.; Shen, P.K.; Shao, Z.; Jiang, S.P. Boosting electrocatalytic activity of single atom catalysts supported on nitrogen-doped Carbon through N coordination environment engineering. *Small* **2022**, *18*, 2105329. [[CrossRef](#)]
80. Liu, D.; Tong, Y.; Yan, X.; Liang, J.; Dou, S.X. Recent advances in carbon-based bifunctional oxygen catalysts for zinc–air batteries. *Batteries Supercaps* **2019**, *2*, 743–765. [[CrossRef](#)]
81. Wei, X.; Luo, X.; Wu, N.; Gu, W.; Lin, Y.; Zhu, C. Recent advances in synergistically enhanced single-atomic site catalysts for boosted oxygen reduction reaction. *Nano Energy* **2021**, *84*, 105817. [[CrossRef](#)]
82. Rozario, A.; Silva e Silva, R.K.; Freitas, M.B.J.G. Recycling of nickel from NiOO/Ni(OH)<sub>2</sub> electrodes of spent Ni–Cd batteries. *J. Power. Sources* **2006**, *158*, 754–759. [[CrossRef](#)]
83. Biesinger, M.C.; Payne, B.P.; Grosvenor, A.P.; Lau, L.W.M.; Gerson, A.R.; Smart, R.S.C. Resolving surface chemical states in XPS analysis of first row transition metals, oxides and hydroxides: Cr, Mn, Fe, Co and Ni. *Appl. Surf. Sci.* **2011**, *257*, 2717–2730. [[CrossRef](#)]

84. Pauletto, P.S.; Florent, M.; Bandoz, T.J. Insight into the mechanism of perfluorooctanesulfonic acid adsorption on highly porous media: Sizes of hydrophobic pores and the extent of multilayer formation. *Carbon* **2022**, *191*, 535–545. [[CrossRef](#)]
85. Ozturk, S.; Xiao, Y.X.; Dietrich, D.; Giesen, B.; Barthel, J.; Ying, J.; Yang, X.Y.; Janiak, C. Nickel nanoparticles supported on a covalent triazine framework as electrocatalyst for oxygen evolution and oxygen reduction reactions. *Beilstein J. Nanotechnol.* **2020**, *11*, 770–781. [[CrossRef](#)]
86. Liang, Y.; Li, Y.; Wang, H.; Zhou, J.; Wang, J.; Regier, T.; Dai, H. Co<sub>3</sub>O<sub>4</sub> nanocrystals on graphene as a synergistic catalyst for oxygen reduction reaction. *Nat. Mater* **2011**, *10*, 780–786. [[CrossRef](#)]
87. Liu, W.; Yu, B.; Liao, X.; Zhao, Y. Facet-Dependent Oxygen Reduction Reaction Activity on the Surfaces of Co<sub>3</sub>O<sub>4</sub>. *Energy Environ. Mater.* **2021**, *4*, 407–412. [[CrossRef](#)]